Master's thesis

NTNU
Norwegian University of Science and Technology

Henrik Gustavson Grytten

How State of Charge Impacts Machine Learning Algorithms for State of Health Estimation of Lithium-ion Batteries.

Master's thesis in Computer Science
January 2022

NTNU
Norwegian University of
Science and Technology

Henrik Gustavson Grytten

How State of Charge Impacts Machine Learning Algorithms for State of Health Estimation of Lithium-ion Batteries.

Master's thesis in Computer Science
January 2022

Norwegian University of Science and Technology

NTNU
Norwegian University of
Science and Technology

Henrik Gustavson Grytten

How State of Charge Impacts Machine Learning Algorithms for State of Health Estimation of Lithium-ion Batteries.

master project, spring 2022

Artificial Intelligence Group
Department of Computer and Science
Faculty of Information Technology and Electrical Engineering

Supervisor Odd Erik Gundersen
Co-supervisor Jacob Joseph Lamb

Abstract

In many real-world applications, only a restricted range of the lithium-ion battery's entire state of charge range is utilized. This is done to preserve the state of health of the battery. Most current research on state of health estimation is not accounting for this fact. Therefore, this thesis is aimed at exploring how the operational state of charge window affects machine learning models for state of health estimation.

In the thesis, a structured literature review that investigates how state of charge impacts state of health estimation is provided. From the findings in the literature review, research questions aimed at expanding the knowledge on this topic were formulated. A methodology for obtaining lithium-ion battery data that can be used to attempt to answer the research questions is presented. Next, two machine learning models capable of predicting state of health parameters were created. These models were analyzed in the context of the state of charge windows the data was extracted from. The results indicated that the state of charge operation window impacts the predictions of the machine learning models. Specifically, a connection between the state of charge operation window and the accuracy of the predictions was observed.

Sammendrag

I mange applikasjoner blir bare en begrenset mengde av litium-ionbatteriers utladnings kapasitet brukt. Dette gjøres for å bedre bevare helsetilstanden til batteriene. Mye av den nåværende forskningen på estimering av helsetilstanden til litium-ionbatterier tar ikke hensyn til dette. Hensikten med denne avhandlingen er å utforske hvordan utladnings mengden til batteriet påvirker maskinlæring modellers evne til å estimere helsetilstanden til batterier.

Avhandlingen inneholder en litteraturstudie med hensikt å identifisere hvordan utladnings tilstanden til batterier påvirker estimering av helsetilstanden. Funnene i litteraturstudiet ble brukt til å formulere forskningsspørsmål. En metode for å anskaffe litium-ionbatteri data som kan brukes med hensikt å svare på forskningsspørsmålene blir presentert. Videre ble to maskinlæring modeller lagd med den hensikt å predikere viktige helseparametere. Disse modellene ble analysert med tanke på hvilke utladnings vinduer batteriene som dataene ble hentet fra var utsatt for. Resultatene indikerte at utladnings vinduet hadde betydning for prediksjonene til modellene. Mer spesifikt ble en sammenheng mellom oppnådd nøyaktighet og utladnings vindu observert.

Preface

This master thesis is the final delivery in the Master's degree program in Computer Science at the Norwegian University of Technology and Science and gives 30 ECTS. Parts of this thesis are repeated and extended from previous work as part of the courses TDT39 and the Specialization Project TDT4501. Repeated work, which may contain some small alterations, from TDT4501 and TDT39 include the *Abstract*, the *Introduction* [Chapter 1] and *Previous Work and Research Questions* [Section 2.4]. Apart from the *Abstract*, the repeated work specified above is from TDT4501, if it is not specifically attributed as work from TDT39. *Background Theory and Motivation* [Chapter 2] except for previously mentioned *Previous Work and Research Questions* [Section 2.4] and *Structured Literature Review* [Section 2.3] has been extensively updated, but much of the work is from TDT4501. *Methodology* [Chapter 3] is previously presented in TDT4501. *Capacity Degradation* [Subsection 4.1.1] and *Capacity Discussion* [Subsection 4.2.2] contains elements previously delivered in TDT4501. *Failed EIS attempt* [Subsection 4.2.1] has previously been delivered in TDT4501.

The master thesis is supervised by associate professor Odd Erik Gundersen and associate professor Jacob Joseph Lamb. The lab work is conducted at the Department of Energy and Process Engineering at the Norwegian University of Technology and Science.

Acknowledgements

Thank you to my supervisor, Odd Erik Gundersen, who agreed to supervise this project and gave insightful feedback. Thank you to my co-supervisor, Jacob Joseph Lamb, for proofreading this thesis and meetings to discuss this project. Thank you to Markus Solberg Wahl for all the help in the lab.

Thank you to Jacob Dahl and Viktor Korsnes for proofreading. Thank you to Torstein, Sander, Markus, Agnar, and Charlotte for the support.

Henrik Gustavson Grytten
Trondheim, June 9, 2022

Contents

List of Figures

List of Tables

Acronyms

AR-ECM Adapted Randles Equivalent Circuit Model. xii, 13, 17, 18, 43, 44, 46, 51

BMS Battery Management System. xii, 1

CCCV Constant Current Constant Voltage. xii, 7, 35–38, 54, 60, 67

CF Capacity Fade. xii

CL Conductivity Loss. xii, 9–11, 17, 18, 42, 43, 45–48, 51

CPE Constant Phase Element. xii, 16–18

ECM Equivalent Circuit Model. xii, 13, 16

EIS Electrochemical Impedance Spectroscopy. xii, 11, 12, 16, 17, 37, 39, 46–51

FCE Full Cycle Equivalent. xii, 7, 51

HPPC Hybrid Pulse Power Characterization. xii

IC Inclusion Criteria. xii

ICA Incremental Capacity Analysis. xii

LAM Loss of Active Material. xii, 9–11, 17, 31, 42, 43, 45–47, 51, 60

LIB Lithium-ion Battery. v, xii, 3, 5–13, 17, 29–36, 39, 42, 43, 48, 49, 51, 52, 54–57, 60, 67–69

LLI Loss of Lithium Inventory. xii, 9–11, 17, 31, 42, 43, 45–48, 51, 60

MAPE Mean Absolute Squared Error. xii

MASE Mean Absolute Scaled Error. xii, 55–60, 67, 68

OCV Open-Circuit Voltage. xii, 8, 11, 30, 31, 35

PF Power Fade. xii

QC Quality Criteria. xii

SEI Solid-Electrolyte Interphase. xii, 7, 10, 17, 18

SHAP SHapley Additive exPlanations. v, xii, 18, 24, 52, 56, 57, 60, 61, 65, 67–69

SoC State of Charge. v, xii, 3, 6, 7, 11, 26–38, 40–42, 50–52, 54, 57, 61, 62, 64, 65, 67–69, 72

SoH State of Health. xii, 1–3, 5–7, 9–11, 26–34, 37, 51, 52, 68–70, 72

SVR Support Vector Regression. xii, 18, 22, 53

Chapter 1

Introduction

Today battery cells are in everyday use as energy storage systems, including mobile applications like cars and stationary applications in electricity grids. Demand for battery cells is expected to rise in the future as battery cells can help decarbonize the transport sector. Decarbonization is an efficient way to combat climate change. In order to use batteries more efficiently, an understanding of battery cells is needed. This understanding is captured in an advanced Battery Management System (BMS). The task of any BMS is to monitor the battery pack and disconnect it from the load in case of an emergency. A sophisticated BMS can also estimate more advanced internal battery parameters and limit the charge and discharge rate. Accurate estimation of these parameters can enhance performance, safety, and durability. Therefore it is important to understand and be able to predict the internal parameters of battery cells. Specifically, knowing the State of Health (SoH) of a battery in operation can be used to improve both safety and durability.

1.1 Background and Motivation

A short review of the SoH estimation topic is provided in [Grytten, 2021] as part of the course TDT39. This discussion is built upon and extended in this section. Currently, SoH estimation is a hot topic in both battery and machine learning research. A review of the most common SoH estimation techniques is given in [Noura et al., 2020]. The publication divides the SoH estimation methods into experimental-based methods and model-based methods. Figure 1.1 provides a overview of the different SoH estimation categories. Experimental methods are based on data collection and analysis of the collected data. This process is often time-consuming and requires specialized equipment. In addition, the

experiments are most likely not possible to conduct in an application of a battery cell. Therefore these methods are not fit for SoH estimation in applications. On the other hand, the experimental methods give a good understanding of the SoH of the test object. The most important parameters can be measured accurately, and good conclusions can be drawn. The model-based methods describe the internal parameters of the target battery under operation. The model's estimates of a selected number of internal parameters are used to estimate the battery's SoH. The most common model-based methods are electrochemical models and equivalent circuit models [Noura et al., 2020]. These methods can be combined with different filters, most commonly a Kalman filter, to increase the estimation accuracy.

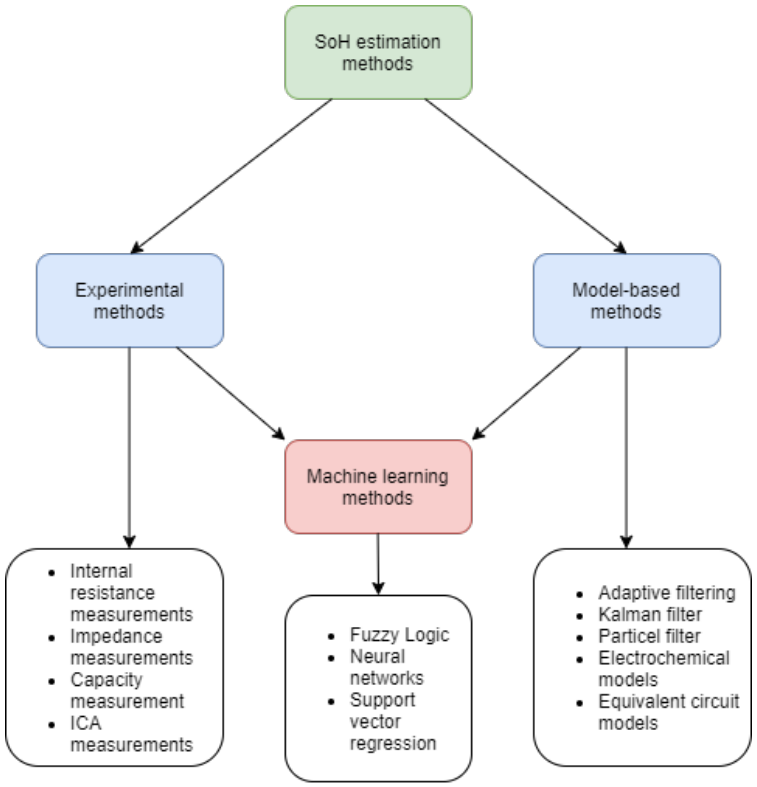

Figure 1.1: Overview of SoH estimation models (adapted from [Noura et al., 2020])

It is common to categorize machine learning methods for LIB SoH estimation as a combination of experimental and model-based methods [Noura et al., 2020]. The source of the data used by the machine learning algorithms can be data from the lab or a real-world application, or it can be data from the battery models. Standard machine learning methods used for state of health estimation are, as discussed in [Grytten, 2021] as part of the course TDT39: "support vector regression [Tan et al., 2020], fuzzy logic [Singh et al., 2004], decision trees, and different types of neural networks like back-propagation neural networks [Yang et al., 2020] and long short term memory neural networks [Li et al., 2020]."
From [Grytten, 2021] as part of the course TDT39: "It is well known that the SoC range a LIB operates in influences its lifetime [Wikner, 2019]. Therefore as a preemptive measure, many devices limit the allowed SoC range before the battery management system disconnects the battery pack from the load. Currently, the most important application where this is done is in battery electric vehicles [Lee et al., 2019]. From the existing literature on battery SoH estimation, it is difficult to say anything about how such particular, but widespread use affects the SoH estimation algorithms compared to most algorithms in the literature, which are created by data from LIB cycled at the complete SoC range."

1.2 Goals and Research Questions

A draft of the research questions has also been discussed in [Grytten, 2021] as part of the course TDT39:

Goal *Provide a better understanding of the SoC window of operation impact on LIB SoH estimation.*

Research question 1 *How does data from a LIB cycled at a specific SoC window affect the accuracy of SoH estimates?*

Research question 2 *Which features are most important for estimating the SoH and does the SoC window impact feature importance?*

1.3 Research Method

The research method used in this thesis has been previously discussed in [Grytten, 2021] as part of the course TDT39: "The research method is a combination of experiments, data analysis, and machine learning model exploration. The experiments are designed to create data that can help answer the research questions. These experiments are relatively simple to set up. Still, they allow us to extract data tailored to help answer the research questions, which is impossible

or difficult to find online. Data analysis is conducted to detect faults in the data and help guide the model exploration. The machine learning models are created to help answer the research questions."

Chapter 2

Background Theory and Motivation

This chapter provides the necessary background theory to understand LIB basic operation and aging. The framework for the working principles of the machine learning model and feature importance attribution technique is described. An overview of the literature review methodology is given. Lastly, the most important findings of the review are identified, and the research objectives are derived from the literature review results.

2.1 Introduction to Lithium-ion Batteries

This section explains the working principles of a LIB. It also covers the main terminology related to LIBs used in this thesis. The section covers the most significant mechanisms behind aging in LIBs. Lastly, different SoH characterization techniques used in this thesis are explained.

2.1.1 Working Principles of Lithium-ion Batteries

A LIB consists of electrodes, a separator, an electrolyte, and current collectors. The positive electrode, during discharge, is defined as the cathode, and the negative electrode is defined as the anode. The separator isolates the cathode and the anode and prevents them from reacting with each other. Ideally, only lithium ions can pass the separator. The current collectors connect the multiple layers of cathodes in parallel and the multiple layers of anodes in parallel. When a load is applied to the current collectors, electrons flow from the anode to the cathode providing power to the load. Lithium atoms are removed from the anode,

become positively charged, and release an electron each. This process is called deintercalation. The electrolyte conducts the lithium ions through the separator to the cathode. At the cathode, during intercalation, lithium is inserted into the cathode structure while obtaining an electron. During charging, the reverse process occurs.

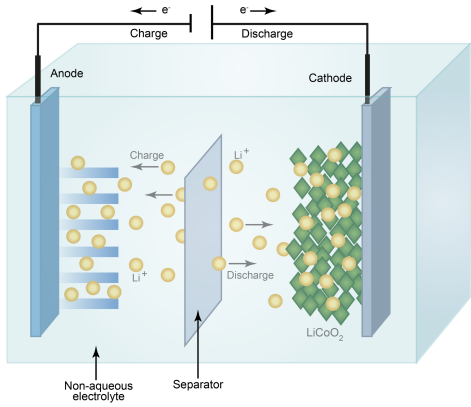

Figure 2.1: Working principles of a LIB (adapted from [Roy and Srivastava, 2015])

2.1.2 Lithium-ion Battery Terminology

This subsection introduces common LIB terminology. These terms are frequently used in the rest of this thesis.

State of Charge

The SoC tells us how much electrical charge is left as a percentage of the LIB's total capacity. At a high SoC, the concentration of lithium in the anode is large. When the SoC lowers, the lithium concentration increases in the cathode and decreases in the anode. The change in lithium concentration lowers the electrical potential of the cathode and increases it in the anode.

State of Health

SoH is a term that describes cell deterioration. A new cell has a 100% SoH. As the cell deteriorates, the SoH is given relative to the original SoH. There is no standard definition of which cell parameters the term SoH refers to, and it

is often chosen depending on the application of the cell. Standard performance parameters to consider are the internal resistance and the cell's capacity.

C-rate

The C-rate is defined as the current out of the cell divided by the nominal capacity of the cell. The C-rate is the term used to describe the current we are applying to the cell. A positive C-rate means that we are discharging, and a negative C-rate means that we are charging. For instance a C-rate of 2 specifies that the LIB is discharged in 30 minutes.

Full Cycle Equivalent

In this thesis a LIB discharge from 100% SoC to 0% SoC and charge back to 100% SoC is referred to as one full cycle. In many instances, LIBs are only partially charged and discharged. The Full Cycle Equivalent (FCE) can be calculated from multiple partial discharges and charges. It is common to use the nominal capacity of the LIB to calculate the FCE. This provides a method to compare LIBs cycled in different SoC ranges.

Constant Current Constant Voltage

Constant Current Constant Voltage (CCCV) is a technique often used during charge or discharge of a LIB when the goal is to end up at a specific open-circuit voltage. A constant current is applied at the start to reach the voltage setpoint quickly. When the target voltage is reached, the current is controlled, either increasing or reducing the LIB's overpotential to keep the measured voltage at the voltage set point. The absolute value of the current necessary to control the overpotential decreases until the current cutoff threshold is reached. The LIB will then approximately have the open-circuit voltage that was targeted.

Solid-Electrolyte Interphase

In LIBs the electrolyte is not stable in the voltage range of the graphite [Pinson and Bazant, 2012]. Therefore the electrolyte decomposes and forms a Solid-Electrolyte Interphase (SEI) layer between the negative electrode and the electrolyte. The SEI layer is created in production during the first few cycles of the LIB. The creation of the SEI layer consumes lithium, and the layer itself increases the LIB's impedance. Therefore, a durable SEI layer that hinders further electrolyte decomposition is crucial for the SoH development of the cell.

2.1.3 Open Circuit Voltage and Overpotentials

The LIB's Open-Circuit Voltage (OCV) is defined as the difference in electrical potential between the cathode and the anode when no load is connected to the LIB, and the cell is in equilibrium. The OCV is dependent on temperature, but most importantly, the state of charge. When current is applied or drawn from a LIB, the LIB experiences overvoltages. These overvoltages are due to the impedance of the LIB. Equation 2.1 gives a typical model of overvoltages, from [Burheim, 2017]:

$$v(t) = OCV(SoC(t)) - i(t)r_{ohmic} - \eta_{ch}(t) - \eta_{diff}(t) \tag{2.1}$$

The most important term in equation 2.1 is $OCV(SoC(t))$ and it is the only term that does not directly depend on the direction of the current. When current is drawn from the LIB, there is an instantaneous voltage drop over the cell caused by the ohmic resistance of the LIB. This is modeled by the term $i(t)r_{ohmic}$. The ohmic resistance is mostly due to resistance in the electrolyte and resistance in other elements such as the current collectors. The ohmic resistance in the electrolyte decreases close to linearly with increasing concentration and decreases close to exponentially with increasing temperature. The η_{ch} in equation 2.1 describes the overvoltage due to electron intercalation and deintercalation in the electrodes. The net current density j of the cell is given by subtracting the cathode reaction, j_c, from the anode reaction j_a:

$$j = j_a - j_c \tag{2.2}$$

At equilibrium electrons are intercalated as quickly as they are deintercalated. From equation 2.2 we observe that at equilibrium j_a equals j_c. The Butler-Volmer equation describes the net current, j, due to intercalation processes:

$$j = j_0 \left(exp\left(\frac{(1 - a_a)\, z\, F}{R\, T} \eta_{ch} \right) - exp\left(\frac{-a_c\, z\, F}{R\, T}\, \eta_{ch} \right) \right) \tag{2.3}$$

j_0 is the exchange current density and is equal to the current density at equilibrium. R is the universal gas constant, F is the Faraday constant, and z is the number of electrons involved in the electrode reaction. a_a is the anode symmetry coefficient, and a_c is the cathode symmetry coefficient. These symmetry coefficients tell us which fraction of the potential between the electrode and electrolyte is used to lower the free energy barrier, allowing reactions, and which fraction influences the current density. The sum of a_a and a_c is by definition always equal to one. The charge transfer overpotential, n_{ch}, occurs because there is a slight resistance, r_{ct}, in the intercalation and deintercalation processes. Therefore, if A

is the surface area of the electrode where electrons can enter and leave, then n_{ch} is given by:

$$n_{ch}(t) = A\, j(t)\, r_{ct} \tag{2.4}$$

η_{diff} accounts for overpotentials due to the diffusion of lithium ions. Fick's first law of diffusion gives us the rate, J, at which lithium ions are transported:

$$J = -D\frac{\partial c}{\partial x} \tag{2.5}$$

In equation 2.5 D is the diffusion coefficient and $\frac{\partial c}{\partial x}$ is the concentration gradient. The diffusion rate and the current created is related by 2.6:

$$J = -zFj \tag{2.6}$$

Combining 2.5 and 2.6 we obtain:

$$\frac{\partial c}{\partial x} = \frac{zFj}{D} \tag{2.7}$$

From 2.7 we observe that the concentration gradient changes linearly in both the electrode and electrolyte, including the interface between them. Therefore, when current is applied to the cell, the lithium concentration decreases at the interface, increasing the overpotential η_{diff}.

2.1.4 Lithium-ion Battery Ageing Mechanisms

The SoH of a LIB decreases both with use and time [Wikner, 2019]. Aging over time is referred to as calendar aging, and aging by usage is referred to as cycling aging. When the SoH of a LIB decreases, both the maximum available power and energy are reduced. This is caused by an increase in internal resistance and a decrease in available capacity [Spitthoff et al., 2021]. This subsection presents the most important LIB degradation modes, the mechanisms causing the degradation and the tools used to identify the different degradation modes.

Lithium-ion Battery Degradation Modes

Studying degradation modes of LIBs greatly simplify aging analysis [Sun et al., 2021]. Degradation modes are usually grouped into Loss of Lithium Inventory (LLI), Loss of Active Material (LAM), and Conductivity Loss (CL) [Pastor-Fernández et al., 2017].

Degradation mode	Important Aging Mechanism
CL	Reduced conduction in the electrolyte current collectors.
LLI	SEI and lithium plating.
LAM	Particle cracking and loss of electrical contact.

Table 2.1: Degradation modes adapted from [Sun et al., 2021]

CL is related to increased ohmic resistance in LIBs. It is caused by a reduced conduction ability in important components of the LIB, such as the electrolyte and current collectors [Sun et al., 2021]. LLI occurs when lithium ions, which are usually transported between the negative and positive electrodes, are consumed by side reactions in the cell. The most important side reactions are lithium plating, formation of metallic lithium, and growth in SEI [Birkl et al., 2017]. LAM refers to the loss of active material which is structures that can intercalate or deintercalate lithium ions. The processes causing LAM differ in the cathode and the anode. LAM in the anode is due to particle cracking, loss of electrical contact, and buildup of resistive surfaces blocking active locations [Birkl et al., 2017]. In the cathode, LAM can be caused by structural disordering, particle cracking, and loss of electrical contact [Birkl et al., 2017].

2.1.5 Lithium-ion Battery Degradation Characterization

Incremental Capacity Analysis

Incremental capacity analysis is an experimental method used to determine the SoH of LIBs. The incremental capacity of a LIB is defined as [Krupp et al., 2020]:

$$IC = \frac{\partial Q}{\partial V}. \tag{2.8}$$

DQDV plots are used to visualize the incremental capacity of LIBs. The incremental capacity is plotted along the y-axis, and the voltage against the x-axis. Figure 2.2 is an illustrative example of a DQDV plot.

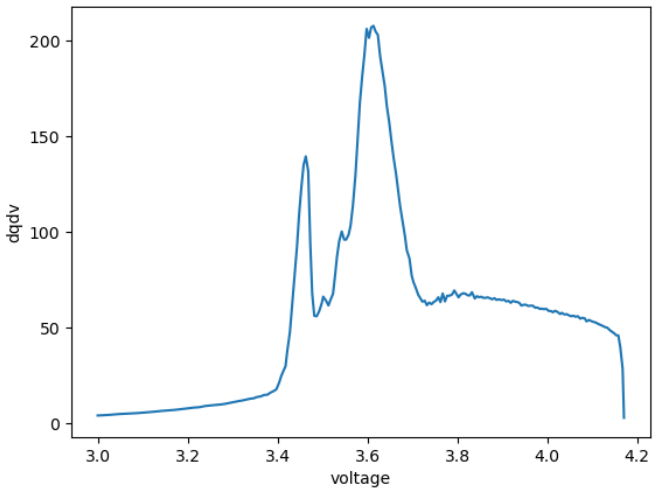

Figure 2.2: DQDV plot

The DQDV plot transforms plateaus in the OCV curve, into clearly separable peaks [Krupp et al., 2020]. This makes is possible to identify the different degradation modes CL, LLI and LAM. CL is related to a shift of the curve toward the lower voltages. LLI manifest itself as lower peaks and peaks shifted either to higher or lower voltages. LAM is observable through decreased high of the peaks, but without the peaks shifting in any direction [Pastor-Fernández et al., 2017], [Dubarry et al., 2012].

Electrochemical Impedance Spectroscopy

Electrochemical Impedance Spectroscopy (EIS) is a technique that measures the frequency response of the impedance of an electrochemical system. The impedance of a LIB depends on, among other factors, the SoC, temperature, and the SoH of the cell. Different frequency intervals of the battery's impedance response can be related to different internal aging processes. EIS works by applying a sinusoidal fixed amplitude and frequency perturbation signal and measuring the response. Given a linear time-invariant system the response will be sinusoidal and phase-shifted with the same frequency as the perturbation signal. Batteries are not linear time-invariant systems, but if the perturbation signal is small, the battery will behave quasi-linearly. This simplification usually gives good results.

The perturbation signal is normally applied multiple times to obtain measurements in a given frequency range. The perturbation signal can be either current or voltage. The galvanostatic mode uses current, and the potentiostatic mode uses voltage as the perturbation signal. The LIB's impedance response at different frequencies can be related to different internal reactions. This enables us to identify different degradation modes during the LIB's aging processes [Pastor-Fernández et al., 2017].

Nyquist Plots

It is common to plot the impedance response obtained from EIS in Nyquist plots. The reason behind this is that the Nyquist plot allows us to easily identify the impedance caused by the negative overpotential terms in equation 2.1. In the Nyquist plot the real part of the impedance response is plotted on the x-axis and the imaginary part is plotted on the y-axis. For the purpose of EIS data analysis we invert the y-axis of the Nyquist plot, simplifying the process of identifying the characteristic shapes of the impedance caused by the different overpotential reactions. The frequency of the impedance response is a sweep parameter where the frequency decreases from left to right. Figure 2.3 is a Nyquist plot of an example impedance response of a LIB. The faster processes inside the LIB are captured at the highest frequencies and appear to the left in the Nyquist plot. The slower internal process are captured by the lower frequency perturbation signals and can be identified to the right in the Nyquist plot. Concretely the ohmic resistance is located in the leftmost part of the plot where the graph of the impedance response crosses the x-axis. The charge transfer process causes the half-circle in the impedance response. The tail of the impedance response at the lowest frequency points is due to the diffusion process.

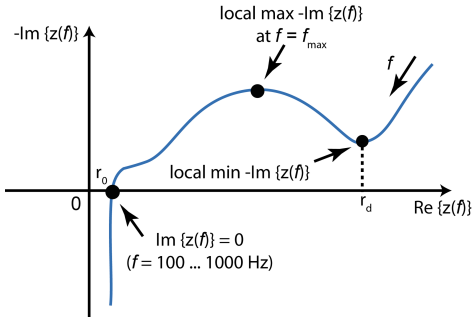

Figure 2.3: Nyquist plot of an example impedance response of a LIB (source [Waag et al., 2013])

Equivalent Circuit Models

We can model the impedance response of a LIB by an Equivalent Circuit Model (ECM). In this thesis, an Adapted Randles Equivalent Circuit Model (AR-ECM) is used. The AR-ECM consists of multiple building blocks connected in series or in parallel. A quick overview of the different components and how they work in relation to each other is given, before the AR-ECM is explained in more detail. Nyquist plots are used to plot the impedance of the different building blocks as it builds a good intuition for how the elements work within the AR-ECM.

Resistors

The impedance of an ideal resistor only contains a real component and is independent of frequency. The impedance is given in equation 2.9 and plotted as a single point on the x-axis in the Nyquist plot in figure 2.4.

$$Z = R \tag{2.9}$$

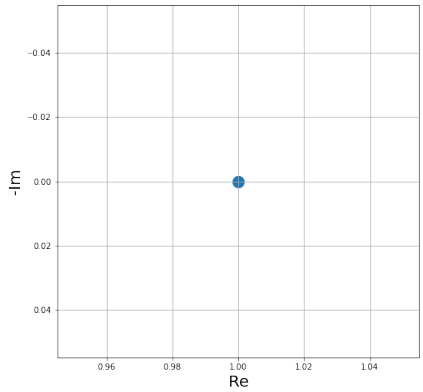

Figure 2.4: Nyquist plot of an ideal resistor

Capacitors

The impedance of capacitors are frequency dependent, as can be seen from equation 2.10. The absolute value of the impedance decreases with frequency. Figure 2.5 plots the impedance of an ideal capacitor.

$$Z(\omega) = \frac{1}{Cj\omega} \tag{2.10}$$

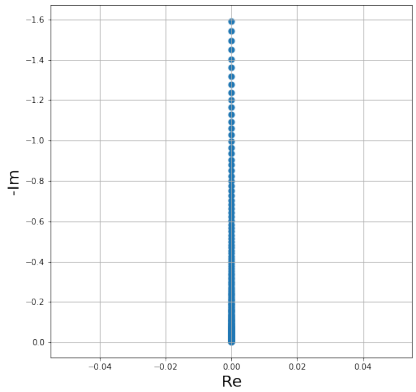

Figure 2.5: Nyquist plot of an ideal capacitor

Resistor and Capacitor in Parallel

By combining a resistor and a capacitor in parallel, more advanced impedance responses can be created. Equation 2.13 gives the impedance of this configuration. It can be observed that the impedance response approaches R as $\omega \to 0$ and 0 when $\omega \to \infty$. In figure 2.6 the impedance response of a resistor and capacitor in parallel is plotted.

$$Z(\omega) = \frac{1}{\frac{1}{R} + \frac{1}{\frac{1}{Cj\omega}}} \tag{2.11}$$

$$\frac{1}{Z(\omega)} = \frac{1}{R} + Cj\omega \tag{2.12}$$

$$Z(\omega) = \frac{R}{1 + Cj\omega R} \tag{2.13}$$

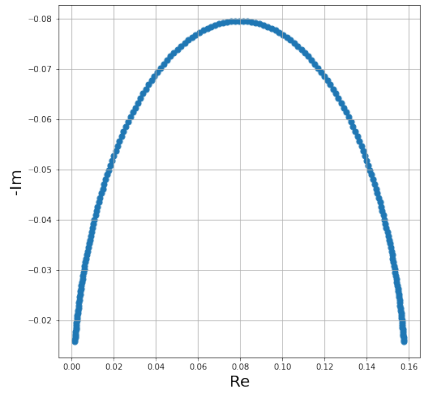

Figure 2.6: Nyquist plot of an ideal resistor and ideal capacitor in parallel

Constant Phase Element and Warburg Element

Equation 2.15 gives the impedance response of a Constant Phase Element (CPE). The impedance is dependent on the frequency ω, in addition to α which determines the phase shift of the CPE. The phase shift of the CPE is given by equation 2.14.

$$\varphi = -\frac{\pi\alpha}{2} \tag{2.14}$$

Setting a equal to one gives a phase shift of $-\frac{\pi}{2}$ and the CPE behaves as an ideal capacitor. If α equals zero, we obtain an ideal resistor. The Warbug element is common in ECMs fitted to EIS data. This is a special case of the CPE where α is equal to 0.5. Figure 2.7 shows the impedance response of a Warburg element.

$$CPE(\omega, \alpha) = \frac{1}{Q(j\omega)^{\alpha}} \tag{2.15}$$

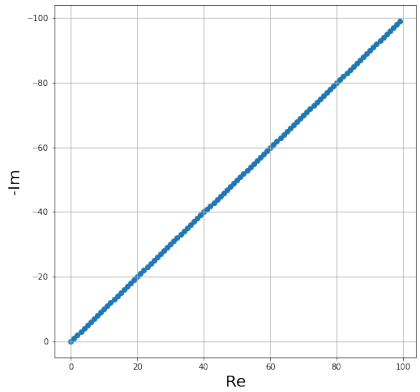

Figure 2.7: Nyquist plot a CPE with α equal to 0.5

Adapted Randles Equivalent Circuit Model

The AR-ECM models impedance of a LIB and can be used to fit a curve to EIS data [Pastor-Fernández et al., 2017], [Zhang and Wang, 2009]. Different components of the AR-ECM models the impedance at different frequency intervals. Specifically the impedance caused by the aging mechanisms SEI, charge transfer and diffusion. These aging mechanisms can be related to the degradation modes CL, LLI and LAM. The growth in percentage metric is introduced in [Pastor-Fernández et al., 2017]:

$$CL_k = \frac{R_{ohm,k} - R_{ohm,1}}{R_{ohm,1}} \cdot 100 \tag{2.16}$$

$$LLI_k = \frac{R_{sei,k} - R_{sei,1} + R_{ct,k} - R_{ct,1}}{R_{sei,1} + R_{ct,1}} \cdot 100 \tag{2.17}$$

$$LAM_k = \frac{R_{w,k} - R_{w,1}}{R_{w,1}} \cdot 100 \tag{2.18}$$

R_{ohm} represents the impedance caused by ohmic resistance, R_{sei} is the resistance cause by SEI, R_{ct} represents the impedance caused by charge transfer, R_w is the impedance caused by diffusion. These equations can be used to calculate the percentage increase in CL, LLI and LAM. The first subscript indicate which AR-ECM component is used to calculate the degradation mode. The second subscript is specifies which EIS experiment is used to calculate the value of the

AR-ECM component. It should be noted that the growth in percentage method is experimental and that there is no trivial one to one way to convert internal aging mechanisms to degradation modes. Figure 2.8 shows the schematics for a AR-ECM. The AR-ECM is composed of resistors, CPEs and a Warburg element. The subscripts in the figure indicate which internal aging mechanism the components are related to. The green components are related to charge transfer, the blue resistor is related to CL, the red components are related to SEI and the yellow Warburg element is related to diffusion according to [Pastor-Fernández et al., 2017].

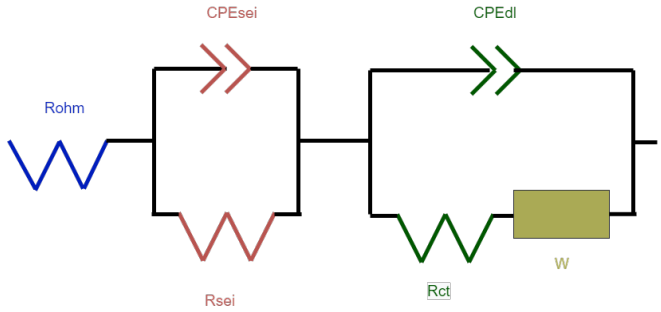

Figure 2.8: AR-ECM (adapted from [Pastor-Fernández et al., 2017])

2.2 Machine Learning

This section gives a quick introduction to time series, which is format of the collected data in this thesis. Basic theory on gradient boosted decision trees and the open source gradient boosting library Catboost is presented. Additionally basic theory on Support Vector Regression (SVR) is provided. Lastly an explanation on how SHAP values can be used to increase the explainability of both gradient boosted decision trees and SVR is given in the respective subsections.

2.2.1 Time Series

This subsection covers the data format of a time series and operations that are useful tools for time series analyses. Lastly Holt's linear method, which is a simple method used for time series prediction, is presented.

Introduction to Time Series

A time series is a set of data points which are ordered in the time domain. There can be many complex patterns in a time series, but some important ones are the trend, the cyclic and the seasonal patterns. A time series has a trend if there is a long-term increase or decrease in the data points over time. Seasonality in the time series is likely to have a fixed and known frequency and its effect on the data is caused by seasonal factors. A cycle is fluctuations that do not have a fixed frequency [Hyndman and Athanasopoulos, 2018]. To better understand to which extent a time series contains trend and seasonality we can analyze the autocorrelation of the time series. The autocorrelation measures the linear dependence between two lagged data points. The autocorrelation in a trended time series should be larger for data points close in time and decrease with increasing time. For seasonal time series, the absolute value of the autocorrelation between data points at a multiple of the seasonal frequency should be large [Hyndman and Athanasopoulos, 2018].

Time Series Decomposition

It is possible to decompose a time series into the described patterns of trend, cycles and seasonality in two ways:

$$y = T + S + R \tag{2.19}$$

$$y = T \cdot S \cdot R \tag{2.20}$$

y represents the entire time series, T is a combination of the trend and cycle patterns, S denotes the seasonality component, and R represents the remainder of the time series. Equation 2.19 is an additive decomposition and equation 2.20 is a multiplicative decomposition. If the level of the time series do not influence the magnitude of the fluctuations caused by the trend-cycle component or the seasonal component, an additive decomposition is prefered over the multiplicative [Hyndman and Athanasopoulos, 2018].

Holt's Linear Trend Method

Holt's linear trend method is a relatively simple time series forecasting method. The method uses two equations to estimate the level and trend of the time series:

$$l_t = \alpha y_t + (1 - \alpha)(l_{t-1} + b_{t-1}) \tag{2.21}$$

$$b_t = \beta(l_t - l_{t-1}) + (1 - \beta)b_{t-1} \tag{2.22}$$

The subscript t indexes the time series at a specific time t. Equation 2.21 is referred to as the level equation. l_t is the estimated level of the time series. a is a tunable parameter and determines how responsive l_t is to recent change in the observed data. y_t is the observed value at time t. l_{t-1} is the last estimated trend and b_{t-1} is the last estimated level. The trend equation 2.22 gives the estimated trend of the y_t. β is a tunable parameter which determines how responsive the trend equation is to change in recently observed data. The forecasting equation is used to predict the time series development:

$$\hat{y}_{t+h|t} = l_t + hb_t \tag{2.23}$$

The forecasting equation 2.23 uses both the level equation and the trend equation in order to make a prediction h time steps ahead of the time index t. The resulting forecast, is composed of the most recent level l_t and a multiple of the most recent trend b_t. Thus the prediction assumes a linear trend development.

2.2.2 Decision Trees

This section introduces the basics of decision trees and uses theory presented in [Mitchell, 1997]. Decision trees are a supervised machine learning method. They are primarily used in solving classification tasks, but can also solve regression problems with great success. Decision trees can be visualized as nodes connected by edges in a tree structure. The input of decision trees is represented as tabular data where each column represents a feature, and each row represents a data point. When solving a classification problem, a specific attribute of the input data is tested at each node in the tree. The result of the test decides the next edge and, therefore, also which attribute is tested next. The algorithm always starts at the root node. It tests attributes and selects a unique path to a leaf node where the input data receives its classification.

The decision tree is built in the learning phase. A statistical test is used to decide which attribute is tested at each node in the tree. The idea is that we want to test the attribute that is most helpful in classifying the input data. To achieve this we use the concept of information entropy. Information entropy is a measure of uncertainty about the possible outcomes of a random variable. The entropy H of our input data X with n different classifications where $P(X_i)$ is the proportion of X belonging to i is given as:

$$H(X) = -\sum_{i=0}^{v} P(x_i)\, \log_2 P(x_i) \tag{2.24}$$

This gives us a measure of the minimum number of bits needed to encode one arbitrary classification. To select which attribute to test next in our decision

tree, we use the concept of information gain. Information gain is the expected reduction in entropy obtained by splitting the input data X by an attribute A. It is defined as:

$$G(X, A) = H(X) - \sum_{v \in V(A)} \frac{|X_v|}{|X|} H(X_i) \tag{2.25}$$

where $v(A)$ are the possible values of attribute A, and $|X_v|$ represents the number of elements in the subset of X with a value v and $|X|$ is the number of input data points. We observe that the second term gives us the expected entropy value after selecting a given attribute to use for partitioning. Every split is done on the feature that maximizes the information gain at that point in the tree.

2.2.3 CatBoost

CatBoost is an open-source python library for gradient boosting using decision trees. Gradient boosting is a machine learning technique that can handle heterogeneous features, noisy data, and complex dependencies in the data [Prokhorenkova et al., 2018]. The algorithm works by iteratively adding weak learners into an ensemble. CatBoost uses binary decision trees as the weak learning model. The idea of gradient boosting is to find a model F that minimizes a loss function $\mathcal{L}(F)$. A data set, D, consisting of n training examples is defined as:

$$D = (x_i, y_i)_{i=1\ldots n} \subset X \times Y \tag{2.26}$$

where the input space, consisting of m input features, is defined as $X = \mathbb{R}^m$ and the output space is defined to be $Y = \mathbb{R}$. Then we can define the loss function as the expected loss of L:

$$\mathcal{L}(F) = E(L(y, F(x))) \tag{2.27}$$

Here L is any differentiable loss function, and the sets y and x consist of independent observations which are identically distributed according to some unknown distribution. This allows the use of an arbitrary smooth loss function which is an improvement over other boosting methods. We build ensemble models F indexed by j by adding weak learners, denoted as w and also indexed by j, in a step by step fashion:

$$F^j = F^{j-1} + \alpha w^j \tag{2.28}$$

α is the step size of the model and is a tunable parameter. We choose the weak learner w^j from the space of weak learners W, by minimizing the loss function:

$$f^j = \underset{w \mathcal{E} W}{\arg\min}\, \mathcal{L}(F^{j-1} + w) \tag{2.29}$$

2.2.4 Support Vector Regression

SVR is a machine learning method used to solve regression problems. The computational complexity of SVR is not dependent on the dimensions of the input space and the method has good capabilities to generalize to unseen data [Awad and Khanna, 2015]. Given a training data set D, as defined in equation 2.26, the objective of SVR is to find a function $f \in \mathbb{R}$ that deviates at most ϵ from every target in $(y_i)_{i=1\ldots n}$ while being as "flat" as possible [Smola and Schölkopf, 2004]. Flatness is desirable because it makes the predictions less sensible to noise in the input.
It is possible for f to be a linear or non linear model. This introduction will be limited to the case where f is a linear function:

$$f(x_i) = \langle a, x_i \rangle + b \quad \text{where} \quad a \in X \wedge b \in \mathbb{R} \tag{2.30}$$

For this linear model, a small a would make the model less sensitive to perturbations in the input features and thus more flat. We therefore wish to minimize the norm of a: $\langle a, a \rangle$. The constraint should be symmetrical in that they do not allow deviations above or below ϵ. This yields the following optimization problem:

$$\begin{aligned} \text{minimize} \quad & \langle a, a \rangle && (2.31)\\ \text{subject to} \quad & y_i - \langle a, x \rangle - b \leq \epsilon && (2.32)\\ & \langle a, x \rangle + b - y_i \leq \epsilon && (2.33) \end{aligned}$$

This optimization problem is not always feasible, because there is not necessarily a function f satisfying the constraints. Two variables ξ and ξ^* are added to the constraint equations making the problem feasible. A term penalizing large ξ and ξ^* is also added to the objective function. The resulting feasible optimization problem is:

$$\begin{aligned} \text{minimize} \quad & \langle a, a \rangle + C \sum_{i=1}^{n} (\xi_i + \xi_i^*) && (2.34)\\ \text{subject to} \quad & y_i - \langle a, x \rangle - b \leq \epsilon + \xi_i && (2.35)\\ & \langle a, x \rangle + b - y_i \leq \epsilon + \xi_i^* && (2.36)\\ & \xi_i \geq 0 && (2.37)\\ & \xi_i^* \geq 0 && (2.38)\\ & C > 0 && (2.39) \end{aligned}$$

A tunable constant C is introduced in the objective function 2.34. C determines to which extent deviations larger than ϵ are penalized and, on the other hand, how flat the resulting function f is.

2.2.5 Shapley Values

Shapley values originate from game theory and can be used in cooperative games to distribute the total payoff among the players, considering each players individual contribution to the payoff. A game has M players. Let F be the set of all players:

$$F = \{1, 2, ..., M\} \tag{2.40}$$

A coalition is a set of players. For every cooperate game we define a function, named the characteristic function, v. The characteristic function assigns a real number to a coalition S, which represents the worth of the coalition S. One must be careful when applying v on a coalition to evaluate the contribution of individual players towards the total gain. This is because the worth increase caused by adding a player i to a coalition can differ depending on which players are already in the coalition. This should not be confused with the worth of a coalition, which only depend on which players are in the coalition, not their order. To determine the contribution of a player i, it is possible to iterate all permutations of F, and find the value i adds to coalitions S, where every player permutated before i in F is a member of S. Let ϕ_i be the contribution of player i:

$$\phi_i = \frac{1}{|F|!} \sum_{P} (v(S \cup \{i\}) - v(S)) \tag{2.41}$$

It can be observed that there are multiple permutations with the same contribution, because the order of the members within S does not matter. There are $|S|!$ permutations of S and there are $(|F| - |S| - 1)$ elements left in F when the elements in $(S \cup \{i\})$ are excluded. Therefore there are $|S|!(|F| - |S| - 1)!$ permutations of elements from F where $\{i\}$ comes after S and the remaining players comes after i. We can rewrite equation 2.41 using these observations:

$$\phi_i = \sum_{S \subseteq F - \{i\}} \frac{|S|!(|F| - |S| - 1)!}{|F|!} (v(S \cup \{i\}) - v(S)) \tag{2.42}$$

ϕ_i in 2.42 is the Shapley value of the player i and gives the average contribution of i in all permutations of F and therefore the contribution player i contributes to the gain of F. Shapley values have some important properties:

1. Efficiency: The total gain equals the sum of all players contribution:

$$\sum_{i=1}^{|F|} \phi_i = v(F) \tag{2.43}$$

2. Symmetry: If $v(S \cup \{i\}) = v(S \cup \{j\}) \quad \forall_{\{S \setminus \{i,j\}\}}$ then $\phi_i = \phi_j$

3. Dummy: If $v(S) = v(S \cup \{i\})$ for every coalition S where {i} is not a member, then $\phi_i = 0$.

4. Additivity: There are two games, one with characteristic function u and one with v. The contribution of i is $\phi_i(u)$ in the first game, and $\phi_i(v)$ in the second game. Because ϕ are Shapley values: $\phi_i(u+v) = \phi_i(u) + \phi_i(v)$.

2.2.6 Shapley Additive Explanations

SHAP is a framework proposed in [Lundberg and Lee, 2017b], that aims to improve the explainability of complex models. SHAP views the input features of the complex model as players in a cooperative game. The framework tries to fairly attribute the prediction of an input instance x made by the complex model to the different input features.

Every distinct feature in the data set is assigned an importance value which tells us to which degree that feature influences the predictions. It works by using multiple simple explanation models. A simple explanation models tries to approximate the output of the complex model F given a single input instance. An additive feature attribution model, g, is defined in [Lundberg and Lee, 2017b]:

$$g(z') = \phi_0 + \sum_{i=0}^{M} \phi_i z'_i \tag{2.44}$$

where $z'_i \in \{0,1\}$ indicates if a feature is observed in the input instance $z' \in \{0,1\}^M$, M is the number of features, and $\phi_i \in \mathbb{R}$ gives each feature an importance value. We know from [Lundberg and Lee, 2017b] that for each input instance x there is always a unique additive feature attribution model g with the three properties local accuracy, missingness, and consistency.

Local accuracy guarantees that given the same input instance z' that g was built from, then $g(z') = F(x)$. Missingness ensures that a missing feature, that is $z'_i = 0$, is given no importance. The consistency property makes it impossible to change a model to increase the impact of a feature while also decreasing the importance the feature is attributed. To illustrate, let $z' \setminus i$ denote setting feature

i of the input instance z' to zero, h_x be a function that maps additive feature attribution model inputs, z', to full model inputs x' and $\phi_i(F, x)$ denote the feature importance of i in a model F and given an input x. Then, according to [Lundberg and Lee, 2017b]:
If

$$F'(h_x(z')) - F'(h_x(z'\backslash i)) \geq F(h_x(z')) - F(h_x(z'\backslash i)) \qquad \forall z' \in \{0,1\}^M \quad (2.45)$$

it follows

$$\phi_i(F', x) \geq \phi_i(F, x) \quad (2.46)$$

[Lundberg and Lee, 2017b] shows that the unique additive feature attribution model g must use Shapely values for feature importance attribution to satisfy the properties of local accuracy, missingness and consistency. Therefore the feature importance of feature i in a model F given input x is:

$$\phi_i(F, x) = \sum_{z' \subset x'} \frac{|z'|!(M - |z'| - 1)!}{M!}(f(h_x(z')) - f(h_x(z'\backslash i))) \quad (2.47)$$

$|z'|$ is the number of non-zero entries in z', and $z' \subset x'$ are all the vectors of z' with non-zero entries that are a subset of the non-zero entries of x'.

Shapley values are the feature importance attribution method that satisfies the consistency property and is preferred over other methods. This example illustrates the importance of the consistency property. Figure 2.9 depicts two decision tree models, model A and model B. The feature "wind" is more critical in model B than in model A. However, a feature importance attribution method lacking the consistency property can assign greater importance to the "wind" feature in model A than in model B. Therefore, it would be problematic to compare the feature importance attributions between the models without the consistency property.

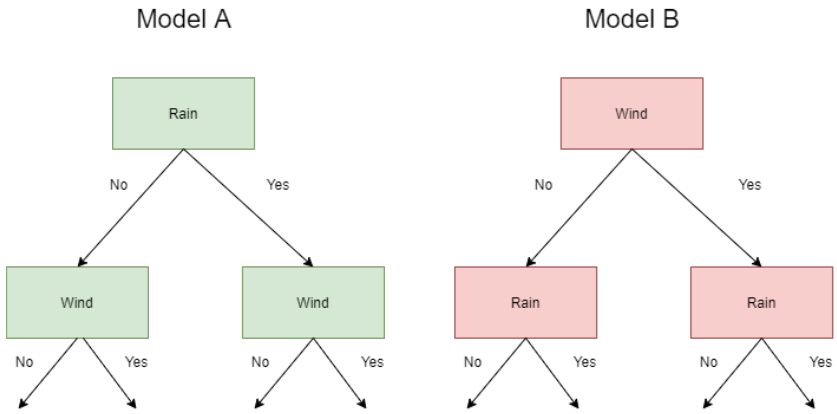

Figure 2.9: Decision tree feature importance comparison (adapted from [Lundberg and Lee, 2017a]).

2.3 Structured Literature Review

A structured literature review was carried out to create research questions and find relevant literature. Some of the work presented in this section has also been discussed in the course TDT39 as part of the research plan [Grytten, 2021]. The literature review was conducted in the Autumn of 2021. The work revealed that there was much research related to both SoH and SoC estimation. Most of this research used equivalent circuits and different state estimation methods. However, there was also a large amount of research in machine learning approaches for estimation of both SoC and SoH. From the literature review, it was clear that there has been much work conducted that tries to relate different operating SoC ranges to different aging mechanics. There is a general agreement that the working SoC range has a large effect on SoH [Wikner, 2019] [Wikner et al., 2021], [Vetter et al., 2005] and [Keil and Jossen, 2016]. Initially, there was not found research about how cycling batteries at constant limited SoC ranges effect SoH estimation for machine learning algorithms. Therefore the focus of the structured literature review was to obtain more information about how the SoC cycle interval affect aging and aging estimation. This led to the search terms given in table 2.3.

2.3.1 Identification of Research

The search engines used and the number of results reviewed in this literature review are listed in table 2.2. Table 2.3 lists the four different search terms and the synonyms that was used for identifying relevant research. There were relatively many results when only search term one, two, and three were employed. Adding the fourth term reduced the number of results in Scopus, IEEE Xplore, and CiteSeerX dramatically and which resulted in much more relevant literature. On the other hand, ScienceDirect continued to give about 100 000 results. Most of these were found not to be relevant, and therefore only the first 100 were included.

Search Engine	**Results reviewed**
Scopus	Every result
IEEE Xplore	Every result
CiteSeerX	Every result
ScienceDirect	First 100 results

Table 2.2: Search Engines

	Synonym 1	Synonym 2	Synonym 3	Synonym 4
Term 1	State of Health	SoH	-	-
Term 2	Battery	Cell	Accumulator	-
Term 3	Estimation	Regression	Approximation	-
Term 4	SoC range	Cycle range	Range	Interval

Table 2.3: Key search terms

2.3.2 Problem, Constraint and Solution Definitions

To concretize the information that was searched for during the literature search, a problem, $\mathcal{P}$, constraints, $\mathcal{C}$ and a solution, $\mathcal{S}$, were defined. The definitions are given in table 2.4. This table defines the problem, $\mathcal{P}$, as the estimation of the SoH of any battery cell. The constraint, $\mathcal{C}$, on $\mathcal{S}$ is that a limited SoC range should be used in solving $\mathcal{P}$. An algorithm or solution $\mathcal{S}$ should be able to give reasonable SoH estimates and be a machine learning method. These definitions were later used to create key search terms and define inclusion criteria and quality criteria.

$\mathcal{P}$	Estimation of the SoH of any battery cell
$\mathcal{C}$	A limited SoC range should be used in solving $\mathcal{P}$
$\mathcal{S}$	A machine learning method should be used in SoH estimation.

Table 2.4: Problem, constraint and solution definitions

2.3.3 Inclusion Criteria and Quality Criteria

The relevant research was identified using the method and parameters given above, but the number of results was too large to handle. Therefore filtering of the results was done. The first filter was that the title of the papers needed to be related to $\mathcal{P}$. The papers that met this criterion are listed in the appendix in table A.5. Next, the selected paper's abstract was scored according to the inclusion criteria. A paper obtained one point for each inclusion criteria it fulfilled. The inclusion criteria were defined using table 2.4 with the goal of narrowing the search and obtaining literature examining SoH estimation using machine learning methods while also taking the SoC window of the data into consideration. Table 2.5 displays the different inclusion criteria. Six of the papers in table A.5 obtained a score of three, indicating that they were highly relevant.

Criteria	**Description**
IC 1	The study is concerned with $\mathcal{P}$.
IC 2	$\mathcal{S}$ is constrained by $\mathcal{C}$.
IC 3	The study provides an $\mathcal{S}$ and an evaluation of how $\mathcal{S}$ performs.

Table 2.5: Inclusion criteria

The last filter that was applied was the quality criteria. The quality criteria are given in table 2.6. These criteria are a form of quality control with regards to the scientific value of the study. All the papers which scored three points based on the inclusion criteria also fulfilled the quality criteria. Lastly, if selection between any obtained studies that were duplicates or appeared in multiple search engines had to be made, the decision was to keep the source with the most quotations.

Criteria	Description
QC 1	The goal of the study is clearly stated.
QC 2	The experiments and results are reproducible.
QC 3	The results of the experiments are analyzed.
QC 4	The paper is written in English.

Table 2.6: Quality criteria

2.4 Previous Work and Research Questions

This section provides a review of related previous work, specifically the highest scoring papers found through the structured literature review: [Lai et al., 2020], [Qu et al., 2019], [Feng et al., 2019], [Lee et al., 2019], [Guo et al., 2021], [Chen et al., 2018] and [Guo et al., 2021]. Afterward, the research questions are described in the context of the previous work. Some of the work presented in this section is also presented in [Grytten, 2021] as part of the TDT39 course.

2.4.1 Review of [Lai et al., 2020]

[Lai et al., 2020] aimed to use machine learning methods to identify the operating SoC windows and temperature of different LIBs. Training and validation data was created in the lab by cycling battery cells at different temperatures and SoC ranges. The extracted features were the incremental capacity curve and the shifts in the curve. The paper concluded that temperature affected the shift in the incremental capacity curve to a larger extent than the SoC range did. On the other hand, the SoC range could in most cases be identified. In this study the accuracy was 67%. It should be noted that the cells were not cycled to end of life, which is typically defined as 80% of the original capacity. Increased aging should, in theory, make it easier to distinguish the cells SoC window and potentially increase the 67% accuracy.

2.4.2 Review of Qu et al. [2019]

A fast online state of health estimation method for LIBs based on incremental capacity curves was developed in [Qu et al., 2019]. The incremental capacity curves were used at the SoC range [0.3−0.8] to estimate SoH. This gave, according to the authors, satisfactory results. The method depended on a linear relationship between the DQDV curve and SoH of the cell. Therefore, the authors found that it was important that the SoC interval used for estimation was in the range of $[0.3 - 0.8]$.

2.4.3 Review of Feng et al. [2019]

In this paper, a support vector machine model was created for online estimation of SoH. The model used incremental capacity curves from partial charging data as input. The particular method which was used in the paper was susceptible to the input SoC. The authors did not investigate to which degree this was due to the underlying aging characteristics of the LIB, or because the method developed required the measured voltage to be monotonic. The authors suggested that an investigation on how the non-uniform aging of the LIB affects the accuracy of the SoH estimation is an exciting topic that requires further study.

2.4.4 Review of Chen et al. [2018]

[Chen et al., 2018] investigated SoH estimation of LIBs using fixed-size least squared support vector machines. The model took discharge time within a given SoC range as input. The paper selected the voltage range $[3.19, 3.25]$ as the optimal SoC range for SoH. The selection process involved comparing the pseudo-OCV curve of three $LiFeP0_4$ cells with different SoH. Different SoC ranges were analyzed to determine in which pseudo-OCV plot the cells were easiest to differentiate. $LiFeP0_4$ is a cell chemistry that stands out from other lithium-ion chemistries in that the OCV curve of the $LiFeP0_4$ chemistry contains a plateau. The voltage range was selected such that the highest voltage was the start of this plateau. This made it easier to separate cells with different SoH in that SoC area. The results stated that the SoH estimation accuracy in general increased with increasing SoC range. [Chen et al., 2018] also found that if the input data contained the upper voltage of the start of the plateau section in the pseudo-OCV curve, it was much easier to obtain good SoH estimates. These results were very specific to the $LiFeP0_4$ chemistry, and the authors suggested that other chemistries should also be investigated.

2.4.5 Review of Guo et al. [2021]

[Guo et al., 2021] is mostly application-focused. Paraphrasing from [Grytten, 2021]: "The authors have created a feature extraction technique aimed at improving SoH estimation in battery applications. The method used only data from the last stage of the charging process where the battery was close to its upper voltage limit. In this stage, the current was applied to control the overpotential caused by the charging current to not exceed the upper voltage limit. This data was much less complex than the discharge data when the battery was used in an application. The authors took advantage of this by training an algorithm and predicting SoH using this algorithm. Multiple features were extracted from the data set, and multiple support vector regression models were trained

using different numbers of features. The models with more features were shown to outperform the models with fewer features in estimating SoH. The data used in this paper was extracted from the end of a charge cycle, and it belonged to a limited and very high SoC range. There was no discussion in the paper about how this affects the extracted features and their relative importance. There was also no mention of how the limited and very high SoC range used for training and estimation could impact performance."

2.4.6 Review of Lee et al. [2019]

This publication is also discussed in [Grytten, 2021] and this review can be considered as an extension of the previous review. [Lee et al., 2019] used data from a limited SoC window to create a SoH estimation algorithm. More specifically, a pseudo-OCV curve was extracted from a limited charging cycle. The paper assumed that the pseudo-OCV data of each of the electrodes were available. That is, both potentials were measured relative to common ground. This is an important simplification that allowed a nonlinear least-squares fit of both of the electrode SoH related parameters. In this case, the chosen parameters were electrode capacity and maximum electrode lithiation. These parameters were tracked as the LIB aged and could be related to LLI and LAM. Multiple models were trained by using different SoC windows as training data. It was not specified in which SoC ranges the LIBs, which the data is extracted from, were cycled. The models were tested on noisy data and compared. The Cram'ser-Rao bound was used as the comparison metric. It provided a best-case lower bound on the variance of the different models. The results showed that the models trained with data from the larger SoC window outperformed models trained on data from smaller SoC windows. It was also evident that data which contained peaks in the DQDV curve and data which contained faster changes in the OCV curve of the electrodes were beneficial for SoH estimation, and thus the SoC operating range was important.

2.4.7 Research Questions

The reviewed papers, specifically [Lee et al., 2019] and [Chen et al., 2018], exemplified that the SoC range has an impact on SoH estimation. The review also indicated that the SoC range of the input data was a significant factor in data-driven models. This was the case in [Chen et al., 2018] where the SoC ranges from the extracted data of the $LiFeP0_4$ cell was crucial for the accuracy, but the results were deemed limited to this type of chemistry due to its special characteristics. [Guo et al., 2021], [Feng et al., 2019] and [Qu et al., 2019] also used limited SoC ranges as input data and concluded that with the specific feature selection conducted in their approaches, the created model accuracy depended on

the input SoC range. They did not however, analyze if the differences in degradation caused by limited SoC windows, had an impact on accuracy. The method described in [Lee et al., 2019] also used data from a limited SoC range. However, it did not take into consideration how this limited SoC range would impact the SoH estimates. The focus of research question one is, therefore, to investigate how different SoC windows impact the accuracy of the machine learning model's SoH estimates by causing various types of degradation: *"How does data from a LIB cycled at a specific SoC window affect the accuracy of SoH estimates?"*
The findings from the review indicated that an analysis of which extracted features from cycling data depend on the SoC for effectiveness is interesting to investigate. Researching the relative feature importance of different extracted features in the context of SoC windows could also yield knowledge about which features are most beneficial for SoH estimation in a given SoC range for machine learning models. This is the motivation behind research question two: *"How does data from a LIB cycled at a specific SoC window affect the accuracy of SoH estimates?"*

Chapter 3

Methodology

This chapter presents the methodology behind the creation of the data used in this thesis. Specifically, the equipment used is described and the aging schedules of all the LIBs are given. In addition, the methods used to characterize SoH are also given.

3.1 Data Acquisition

The data needed to answer the research questions is very specific. The LIBs used needed to be cycled within a certain SoC window. It was also necessary to run an extensive characterization of the cycled LIB at given intervals. This data was not easily obtainable from public databases. Therefore a data-set tailored to this project was created by aging four LG-Chem JP3 LIBs. The cells are numbered from one to four and their corresponding SoC range is given in table 3.4.

3.1.1 Equipment Specification

LG-Chem JP3 is 64 Ampere hour LIB with 3.0V lower cutoff and 4.2V upper cutoff voltage. A battery cycler, a temperature chamber, and a potentiostat were utilized for cycle aging and SoH characterization of the LIB. The battery cycler was an Arbin Instruments MitsPro8. This instrument can deliver large currents while still having a high current and voltage measurement accuracy. Two channels of the Arbin Instruments MitsPro8 were used for each cell and connected in parallel. This enabled charge and discharge rates of 60 amperes and allowed faster aging than what a single channel would achieve. A low accuracy auxiliary temperature measurement device provided ambient temperature measurements

and was an important safety feature. The specifications of the Arbin Instruments MitsPro8 are given in table 3.1.

Specification Type	Specification
Max channel current	± 30 A
Current measurement accuracy	± 0.012 A at 30 A ± 0.002 A
Voltage measurement accuracy	± 0.002 V

Table 3.1: Arbin Instruments MitsPro8 Specifications

The potentiostat was used for SoH characterization and was a Gamry Interface 5000. Table 3.2 gives the specifications and measurement accuracy of the Gamry Interface 5000 using the galvanostatic mode.

Specification Type	Specification
Max voltage measurement error	8.9 mV
Max current measurement error	12.5 mA

Table 3.2: Gamry Interface 5000 Specifications

As the temperature impacts the parameters of LIBs, it was important to control the ambient temperature. Therefore the four LG-Chem JP3 LIBs were cycled in two temperature chambers from VWR. The temperature chamber model was IL 68R. Table 3.3 gives the specifications of the temperature chambers used.

Specification Type	Specification
Temperature range	3 - 70°C
Temperature accuracy	± 0.1 °C at 37 °C

Table 3.3: VWR IL 68R

3.1.2 State of Charge Windows

In this project, the LIBs were cycled in different SoC ranges. The four different SoC windows were 10-90%, 35-65%, 20-50% and 65-95% and are illustrated in figure 3.1. These ranges allow comparison of the aging at different limited voltage ranges, in addition to one cell aging at almost the full range. At the start of the

project, a pseudo-OCV curve was found by discharging the batteries at a rate of C / 30 . By using this data, the upper and lower voltages of the different SoC windows were calculated. These points are given in table 3.4.

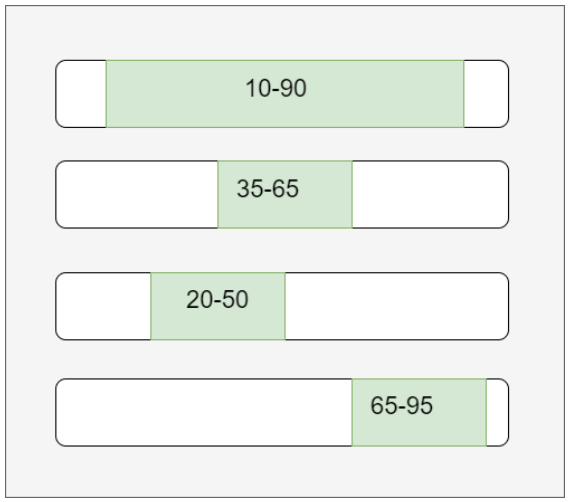

Figure 3.1: SoC windows

Cell number	SoC window	Lower voltage	Upper voltage
Cell 1	10-90%	3.457 V	4.032 V
Cell 2	20-50%	3.535 V	3.659 V
Cell 3	35-65%	3.779 V	3.607 V
Cell 4	65-95%	4.092 V	3.779 V

Table 3.4: Cell Identifiers and Voltage Windows

3.1.3 Lithium-ion Battery Ageing Schedule

An aging schedule for each of the four LIBs cycled in this project was created. During aging, the temperature chambers were set at 35°C. It is important to keep the LIBs SoC working range within the specified limits. Therefore, to reach the upper SoC limit when charging, CCCV charging mode was utilized until the upper voltage limit was reached, as defined in 3.4. At discharge, constant current was used for a specified duration in order to reach the lower SoC limit. Data from

this part of the aging schedule is plotted in figure 3.2. Every tenth aging cycle is special. During discharge, at each 10% SoC interval, an internal resistance measurement was conducted automatically by the Arbin Instruments MitsPro8 battery cycler. Before an internal resistance measurement, the scheduler paused for 10 minutes, allowing the LIB to be closer to equilibrium. Typical voltage and current data from this step is plotted in figure 3.3.

Aging Schedule

1. Discharge with constant current for a specified duration at 0.9375 C.
2. Rest 10 minutes at the lower SoC limit.
3. CCCV charge at 0.9375 C to the upper voltage limit with cutoff at 0.1 C.
4. Rest 10 minutes at the upper voltage limit.
5. Increment the cycle counter.
6. Go to step 1 if the cycle counter is divisible by 10. Else go to step 7.
7. Measure the internal resistance.
8. Discharge 10% of the total LIB SoC window with 1 C constant current.
9. Rest for 10 minutes.
10. Measure the internal resistance.
11. Go to step 3 if the lower SoC limit is reached. Else go to step 8.

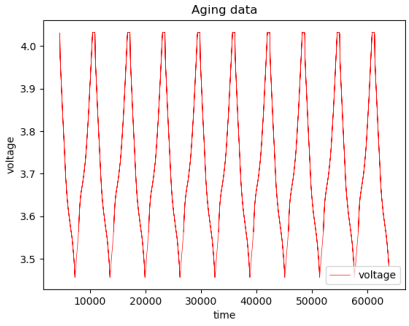

(a) Voltage from cycling in the 10%-90% SoC range

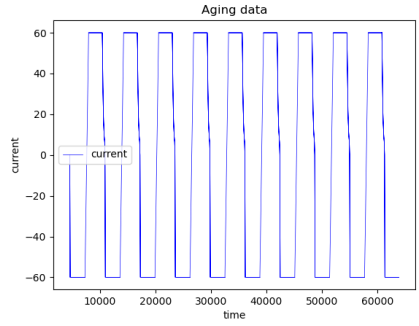

(b) Current from cycling in the 10%-90% SoC range

Figure 3.2: Aging schedule data

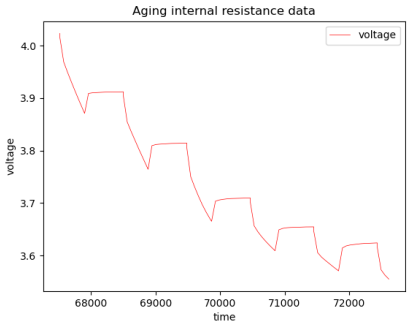

(a) Voltage from internal resistance characterization cycling in the 10%-90% SoC range

(b) Current from internal resistance characterization cycling in the 10%-90% SoC range

Figure 3.3: Internal resistance measurements

3.1.4 Lithium-ion Battery State of Health Characterization Schedule

Once a month, a SoH characterization was conducted. This was done with the temperature chamber at 25°C. During characterization, multiple capacity tests were run at different C-rates. In addition EIS was conducted. The schedule for the EIS and capacity tests is given in the tables below.

Electrochemical Impedance Spectroscopy

1. CCCV charge to 100% SoC at 60C/64 with cutoff current of C/10.
2. The potentiostat mode to galvanostatic mode.
3. The frequency range is 0.1 MHz to 0.1 Hz.
4. The number of points per frequency decade is 100.
5. The perturbation current amplitude is 3A.

Capacity tests

Capacity Test C/10:

1. Discharge at C/10 constant current until 0% SoC is reached.
2. CCCV charge at C/10 with cutoff current of $\frac{6.3}{64}$ C.
3. Rest 10 minutes after charge.

Capacity Test C/3:

1. Discharge at C/3 constant current until 0% SoC is reached.
2. CCCV charge at C/3 with cutoff current of C/10.
3. Rest 10 minutes after charge.

Capacity Test C/2:

1. Discharge at C/2 constant current until 0% SoC is reached.
2. CCCV charge at C/2 with cutoff current of C/10.
3. Rest 10 minutes after charge.

Capacity Test C/1:

1. Discharge at 60C/64 constant current until 0% SoC is reached.
2. CCCV charge at 60C/64 with cutoff current of C/10.
3. Rest 10 minutes after charge.

Chapter 4

Battery Aging Results and Discussion

This chapter presents the results from the LIB aging schedule. Raw data is presented, in addition to some analysis that attempts to capture the different degradation modes of the individual LIBs. Lastly, the obtained results are discussed and compared between the different LIBs.

4.1 Aging Results

The results of the aging of the four tested cells is presented in this section. The results originates from the discharge tests, internal resistance measurements and the EIS experiments.

4.1.1 Capacity Degradation

This subsection contains results from the capacity tests described in 3.1.4. Table 4.1 gives the calculated capacity degradation obtained from the C/2 tests of all the 4 tested cells. Figure 4.1 plots the discharge curves used to calculated the values in table 4.1.

Characterization	10-90% SoC	20-50% SoC	35-65 SoC	65-95% SoC
1	100%	100%	100%	100%
2	97.2%	99.9%	98.7%	97.5%
3	94.9%	99.3%	97.7%	95.7%
4	92.7%	98.7%	97.0%	94.5%
5	90.7%	98.3%	96.5%	93.5%
6	89.2%	97.8%	95.9%	92.8%

s

Table 4.1: Capacity decrease from C/2 discharge tests

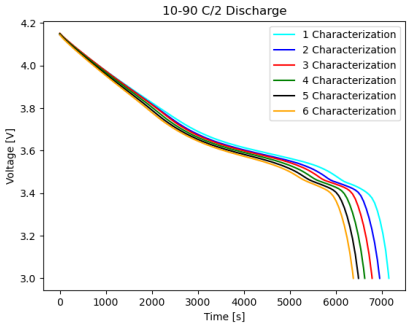

(a) Cell 1 2C discharge.

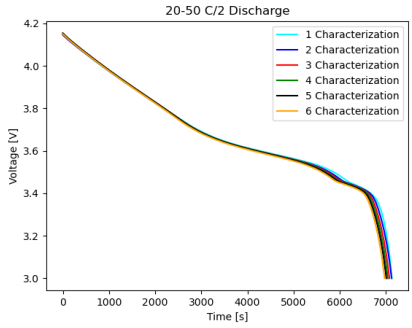

(b) Cell 2 2C discharge.

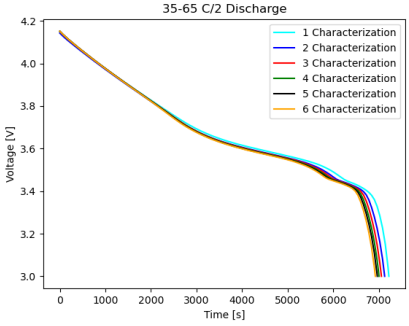

(c) Cell 3 2C.

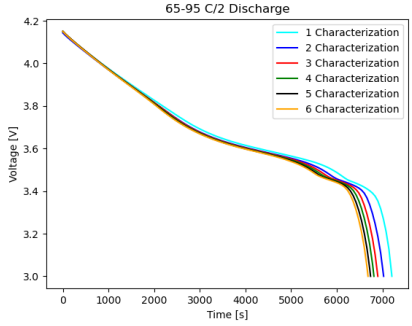

(d) Cell 4 2C discharge.

Figure 4.1: 2C discharge curves

Table 4.2 contains the calculated capacity degradation obtained from the C/10

Characterization	10-90% SoC	20-50% SoC	35-65 SoC	65-95% SoC
1	100%	100%	100%	100%
2	97.5%	97.7%	97.3%	95.7%
3	96.7%	98.4%	97.7%	95.8%
4	94.5%	97.7%	96.8%	94.5%
5	91.3%	96.1%	95.2%	92.3%
6	89.6%	95.7%	94.6%	91.6%

Table 4.2: Capacity decrease from C/10 discharge tests

tests of all the 4 tested cells. Figure 4.2 displays the discharge curves used to calculate the values in table 4.2.

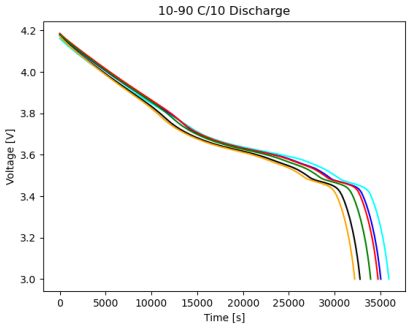

(a) Cell 1 10C discharge.

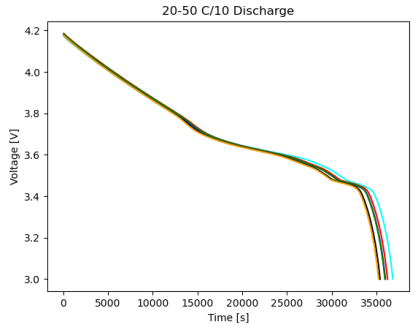

(b) Cell 2 10C discharge.

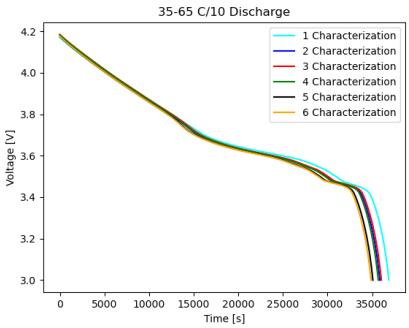

(c) Cell 3 10C discharge.

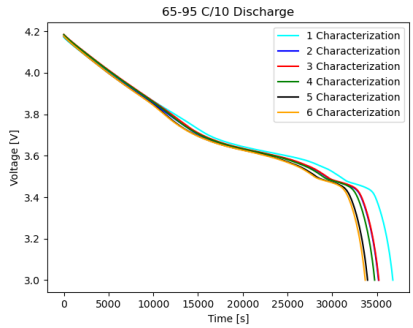

(d) Cell 4 10C discharge.

Figure 4.2: 10C discharge curves

4.1.2 Internal Resistance

This subsection contains results from the internal resistance tests as described in subsection 3.1.3. The tests were automated and ran multiple times a day by the Arbin Instruments MitsPro8. As explained in subsection 3.1.3, the internal resistance at every 10% SoC interval was measured every tenth aging cycle. For simplicity, figure 4.3 plots the average of the measurements taken at 10% SoC intervals over the entire test period.

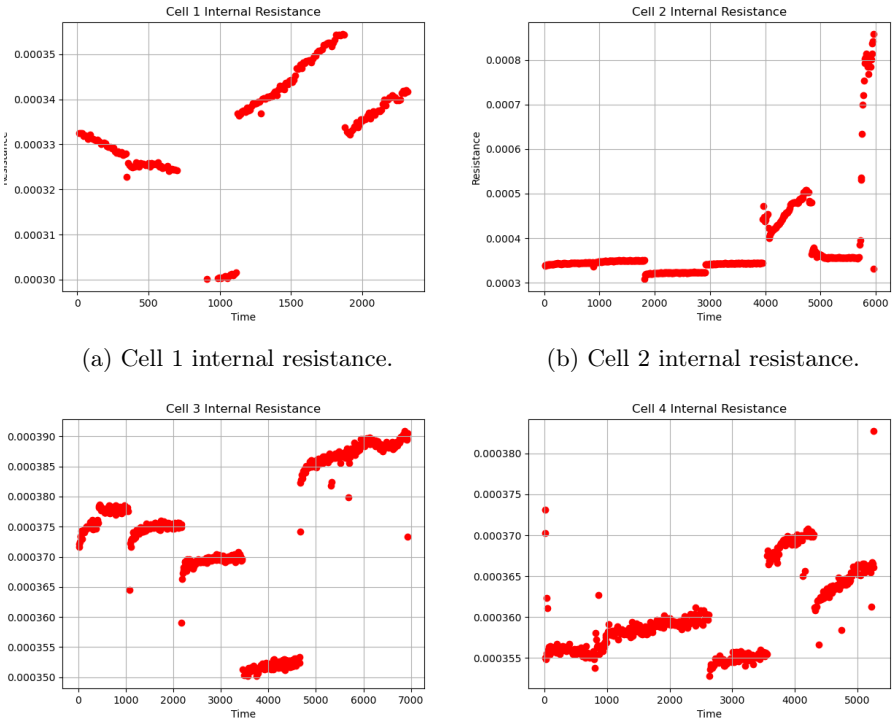

(a) Cell 1 internal resistance.

(b) Cell 2 internal resistance.

(c) Cell 3 internal resistance.

(d) Cell 4 internal resistance.

Figure 4.3: Measured internal resistance

4.1.3 Degradation Modes Characterization

The aim of this subsection is to characterize the degradation modes, CL, LAM and LLI of the tested LIBs. The general trend of the degradation modes is considered. Therefore, for simplicity, the first successful experiments conducted in November

2021 and the last experiments conducted in March 2022 are compared. The following subsections utilizes AR-ECMs to model the impedance responses of all the tested LIBs. The AR-ECMs are created and the results are plotted using the python package "impedance.py" [Murbach et al., 2020]. As described in 2.1.5, the percentage increase of the degradation modes are calculated from the models. The DQDV curves obtained in November 2021 and March 2022 are also analyzed to provide more information on the evolution of the different degradation modes. In this subsection, all the data plotted in blue originates from November 2021, and all the data plotted in orange originates from March 2022.

Cell 1 Degradation Modes

Figure 4.4a shows the curve fit of the impedance response in November and 4.4b plots the curve fit of the impedance response in March. The calculated change in degradation modes from these curve fits are given in table 4.3.

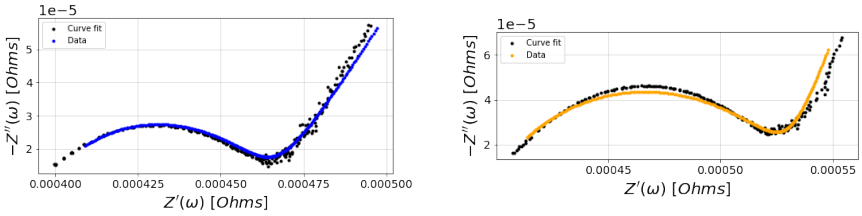

(a) EIS measurement cell 1 November 2021 (b) EIS measurement cell 1 March 2022

Figure 4.4

Table 4.3 shows a small increase in CL, a small decrease in LAM and a quite large increase in LLI. Figure 4.5 plots the DQDV curves from November 2021 and March 2022. There is no significant voltage shift towards lower voltages, indicating no significant change in CL. The peak of the curve is reduced quite a lot, in addition to some reduction at approximately 3.45[V]. This indicates LAM. The relative minimum at approximately 3.75[V] is shifted to the right from November 2021 to March 2022. This change is most likely due to LLI.

Characterization Time	CL[%]	LLI[%]	LAM [%]	Curve fit MASE [%]
November 2021	0	0	0	0.39
March 2022	0.8	92.7	11.3	0.45

Table 4.3: Percentage change in degradation mode for Cell 1

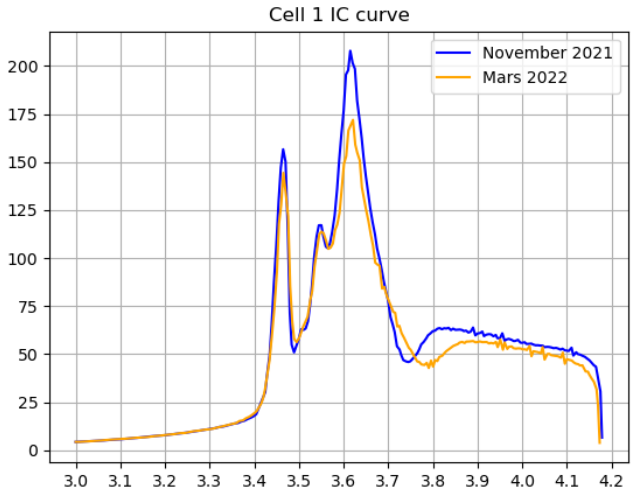

Figure 4.5: Incremental capacity curves for cell 1

Cell 2 Degradation Modes

Figure 4.6a shows the curve fit of the impedance response in November 2021 in a Nyquist plot. Figure 4.6b shows the curve fit of the impedance response in March. We observe that, over time and aging, the tail of the graph, typically related to diffusion, changes direction. The AR-ECM is not suited to handle this development, and the curve fit is therefore a bit off in this section of the graph.

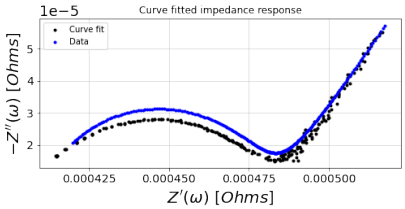

(a) EIS of Cell 2 November 2021

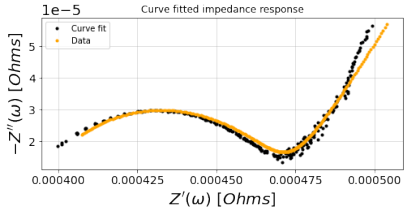

(b) EIS measurements Cell 2 March 2022

Figure 4.6

Table 4.4 shows the percentage growth of the different degradation modes for

cell 2. We observe that there is a small decrease in CL and small increases in LLI and LAM over the cycle time of the cell.

Characterization Time	CL[%]	LLI[%]	LAM [%]	Curve fit MASE [%]
November 2021	0	0	0	0.42
March 2022	-4.5	12.5	4.3	0.36

Table 4.4: Percentage change in degradation mode for Cell 2

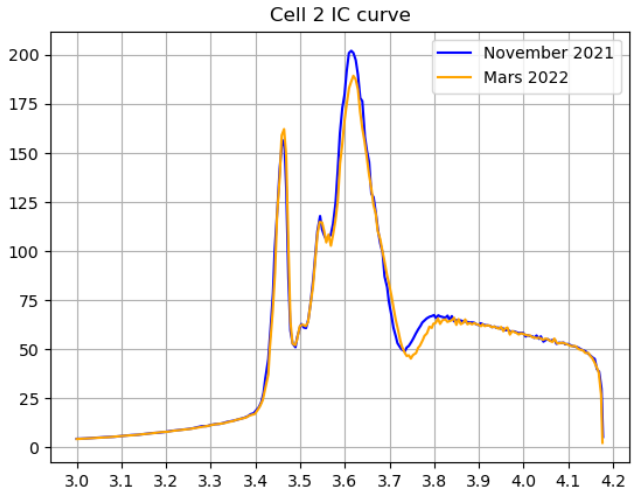

Figure 4.7: Incremental capacity curves for cell 2

Figure 4.7 plots the DQDV curves from November 2021 and March 2022. There is no significant shift towards lower or higher voltages indicating no significant increase or decrease in CL. At about 3.75[V] there is a small shift and decrease in the DQDV curve, indicating some LLI. There is a small decrease in the DQDV curve at approximately 3.6[V] indicating a small decrease in active material.

Cell 3 Degradation Modes

Figure 4.8a plots the EIS measurements in black and curve fit in blue from November 2021 in a Nyquist plot. Figure 4.8b shows the curve fit of the impedance response in March. As with cell 2, we observe that the tail of the graph, typically related to diffusion, changes direction. The AR-ECM is not suited to handle this development, and the curve fit is therefore not optimal in this section of the graph.

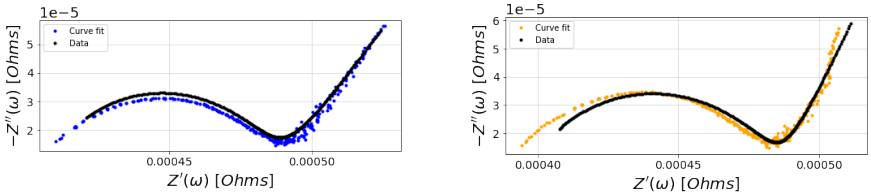

(a) EIS measurement cell 3 November 2021 (b) EIS measurement cell 3 March 2022

Figure 4.8

Table 4.5 shows that there is not to much change in the estimated degradation modes CL, LLI and LAM. This agrees with the DQDV plot in figure 4.9. The DQDV plot does not show any significant left shift, which would indicate CL. There is however some indication of LAM due to the right shift of the relative minimum at about 3.7[V]. The decrease peak at about 3.6[V] indicates some LAM.

Characterization Time	CL[%]	LLI[%]	LAM [%]	Curve fit MASE [%]
November 2021	0	0	0	0.26
March 2022	-2.8	15.3	9.6	0.43

Table 4.5: Percentage change in degradation mode for Cell 3

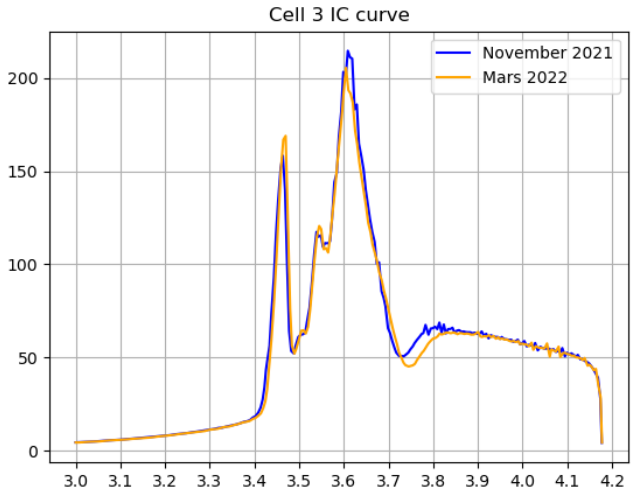

Figure 4.9: Incremental capacity curves for cell 3

Cell 4 Degradation Modes

Figure 4.10a and 4.10b plots the EIS measurements and curve fits from November 2021 and March 2022. Figure 4.10b shows the curve fit of the impedance response in March. Table 4.6 gives the percentage change in the degradation modes from the first to last measurement. A small increase in CL and LAM can be observed, in addition to a relative larger percentage increase in LLI.

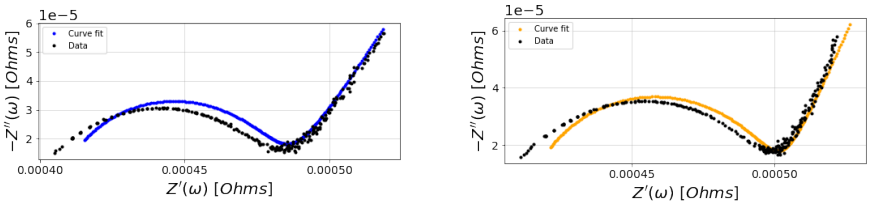

(a) EIS measurement cell 4 November 2021 (b) EIS measurement cell 4 March 2022

Figure 4.10

Characterization	CL[%]	LLI[%]	LAM [%]	Curve fit MASE [%]
1	0	0	0	0.34
5	1.8	17.1	6.1	0.39

Table 4.6: Percentage change in degradation mode for cell 4

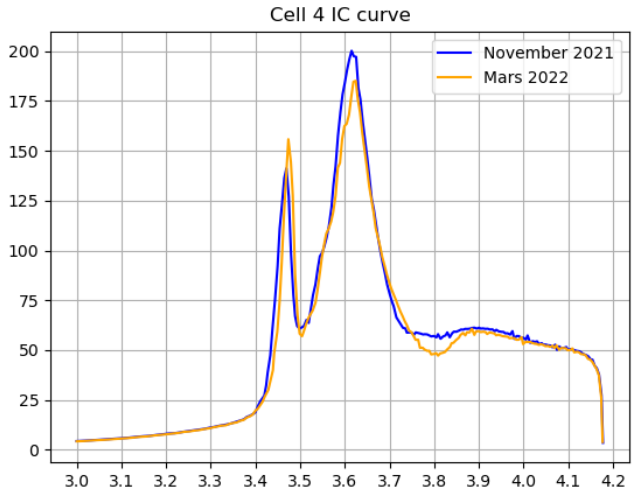

Figure 4.11: Incremental capacity curves for cell 4

The DQDV plot in figure 4.11 does not display any significant left shift, which would indicate CL. The peak observable at about 3.45[V] is actually larger in the aged cell, then when the cell was new. The next peak at about 3.6[V] and the relative minima at about 3.7[V] is lowered and shifted which indicate LLI.

4.2 Result Discussion

The following subsection discuss the first EIS attempt, which failed due to noise in the data. The measures taken to improve the data quality are described. Next, the observed capacity loss, the internal resistance measurements and the degradation modes obtained by the LIB characterization techniques are discussed.

4.2.1 Failed EIS Attempt

During the project, a total of six EIS measurements were done. Only five of these experiments were successful. This subsection covers the failure in the first EIS measurements and the actions taken to improve the measurements. Figure 4.12 plots the measured impedance from this first characterization in a Nyquist plot. The measurements were very noisy. It was difficult to identify the reason for the noisy data, and it was probably caused by a combination of issues. Firstly the EIS equipment was tested and verified using a much smaller LIB of 6.55 Ah rated capacity. Smaller cells typically have more impedance than larger cells because fewer electrodes are connected in parallel internally. This means that the root mean square value of the perturbation signal can be less for the smallest cell. A smaller perturbation signal reduces the electromagnetic noise during the experiment. The possible impact of electromagnetic interference was not well understood by the author at the time of the first EIS characterization. Therefore the signal cable and the measurement cable of the EIS were not separated at all. Secondly, the perturbation signal was increased when measuring the impedance of the larger cells, but probably not enough. In addition, by inspecting figure 4.12, it is clear that the ohmic resistance, along the x-axis, is about a hundred times higher than the actual internal resistance of the cells. This indicates that there may have been a bad electrical connection between the LIB and the test equipment.

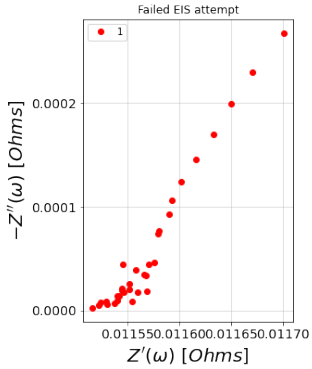

Figure 4.12: Failed EIS attempt

The second EIS characterization gave usable data. Figure 4.13 plots one of the impedance responses of one LIBs in a Nyquist plot. The shape of the curves is comparable to the shape of the Nyquist plot in 2.3. Measures taken from the first

attempt to the second attempt were to separate the signal and measurement cables of the EIS equipment as much as possible, ensure good electrical connection, increase the number of sampling points and increase the perturbation current from 0.5A to 3A.

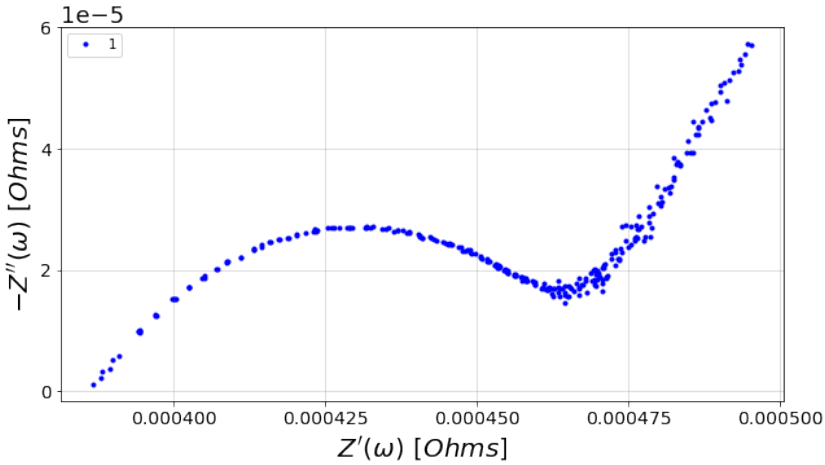

Figure 4.13: Usable electrochemical impedance spectroscopy measurement

4.2.2 Capacity Discussion

The results from both the C/2 discharge test and C/10 discharge test are given in subsection 4.1.1. The calculated capacity degradation given in tables 4.1 and 4.2 are within the variation we can expect. We observe that cells 1 and 4, which were cycled at higher SoC ranges, are subject to a larger amount of capacity decrease when compared to cells 2 and 3 which were cycled at lower SoC ranges. This is expected according to [Gao et al., 2018]. By looking at the capacity degradation from both cell 1 and cell 4, it is evident that cell 1 experienced a larger capacity

decrease. On the surface this is a bit unexpected, as the upper SoC range should effect capacity decrease more than lower SoC ranges. However the charge and discharge time of cell 1 was longer than the charge and discharge time of cell 4. The reason is that cell 1 was cycled in the 10%-90% SoC range and cell 4 was cycled in the 65%-95% SoC range. Since the rest time, 10 minutes, was equal for both cells, this led to cell 1 having more FCE than cell 4 in addition to cells 2 and 3. This can explain the increased capacity loss of cell 1.

4.2.3 Internal Resistance Discussion

LG-Chem JP3 is a 64 Ampere hour LIB with many internal cathodes and anodes connected in parallel. This results in a LIB with very low internal resistance. As the resistance decreases, obtaining accurate measurements becomes more difficult and effects that are negligible in other LIBs becomes increasingly important. Looking at the measured internal resistance of the 4 LIBs in figure 4.3, it is clear that the Arbin Instruments MitsPro8 was unable to accurately determine the internal resistance. We can assume that all the internal resistances were between about 0.3 and 0.4 m[Ω], but the data is not good enough to be useful. By inspecting the plot in figure 4.3, it is clear that in many measurements there were a bias that changed with a period of about one month. This matches the time of when the SoH characterization schedule was executed. During this procedure, the cells were disconnected from the cycler to obtain the EIS measurements, before they were reconnected. It is reasonable to assume that the change in internal resistance is negligible before and after the SoH characterization schedule. Therefore the periodically changing bias, which seems to have been the most important factor in ruining the measurements, was probably due to tiny differences in the electrical wiring connecting the cells to the cycler.

4.2.4 Degradation Modes Discussion

Two methods were utilized to characterize the degradation modes of the cells. The method of analyzing DQDV curves is more established than the EIS approach where the AR-ECM is utilized. Therefore, if there are any discrepancies, the DQDV curve is likely to be more accurate. Common for all 4 LIBs was that there seemed to be little change in CL. By looking at the AR-ECM results it seems that the dominating degradation mode for all 4 cells is LLI. Inspection of the DQDV curves indicates that this is a good assumption for cell 2, 3 and 4. For cell 1 on the other hand, it seems that LAM also was a significant degradation mode.

Chapter 5

Machine Learning Models

This chapter describes the objective of the machine learning models used in this thesis. A quick description of the two selected model designs is given. The input features of the models are explained. Next, the methodology used to train and validate the two models is elaborated. Lastly, the method for calculating SHAP is given.

5.1 Model Objective

The models are built to investigate research question 1, how the SoC windows affects the SoH estimates, and research question 2, how the SoC windows influences feature selection for the SoH estimation, as defined in section 1.2. To achieve this, the models, in general, need to be accurate at predicting the SoH, and it should also be possible to infer to which degree the different input features influence the predictions. One challenge with this problem description, as explained in 2.1, is that there is no standardized definition of the concept of a SoH in LIBs. However, resistance and capacity degradation are common parameters used when evaluating SoH. Unfortunately, the Arbin Instruments MitsPro8 was not able to measure the development of the resistance during testing. Therefore the models are limited to predicting the capacity degradation of LIBs.

5.2 Models

For comparison reasons, this thesis uses two machine learning models to make SoH predictions. Model 1 is based on Holt's linear method combined with the open-source library Catboost. Model 2 utilizes Holt's linear method in combi-

Model	Architecture
Model 1	Holt's linear + Catboost
Model 2	Holt's linear + SVR

Table 5.1: Model architecture

nation with scikit-learn's implementation of SVR [Pedregosa et al., 2011]. Table 5.1 list the models and their respective architecture.

Hybrid models increase model complexity, but in both cases, increased model performance was achieved by Holt's linear method. This result is expected in the case of model 1, as gradient boosted decision trees are inherently inefficient at predicting time series with a trend. The accuracy increase is a bit more unexpected in the case of model 2 since SVR is better equipped to handle trends. A data set D, as defined in equation 2.26, is needed to train the models. Both models train by decomposing the target input training data $(y_i)_{i=1..n}$ in D using Holt's linear method. The result is two-time series l and t, where l represents the level, and t represents the trend of the target. In model 1, a "CatboostRegressor" is fitted with the level series l as the target. Likewise, in model 2, a support vector regressor is fitted to l. When making predictions with both models, an equation similar to the forecasting equation 2.23 in Holt's linear is used:

$$\hat{y}_{t+h|t} = m_h + hb_t \tag{5.1}$$

$\hat{y}_{t+h|t}$ represents the forecast h time steps ahead. The term hb_t predicts a linear trend where b_t is the estimated trend of Holt's linear method. In model 1, m_h represents the predicted output of the "CatboostRegressor" at index h. In model 2, m_h represents the predicted output of the SVR at time step h.

5.3 Feature Extraction

The features used in the models in this thesis are selected based on their predictive ability. In [Severson et al., 2019], a simple but accurate predictive model was built using features extracted from discharge curves and their derivatives. Therefore, many of the features extracted in this thesis are also based on this approach. From the DQDV curve of the discharge step in the aging schedule, the peaks from the DQDV curve are extracted using the function "argrelextrema" from [Virtanen et al., 2020]. In addition, the relative time between the peaks is calculated. In figure 5.1, an example DQDV curve is plotted. The green dots represent the local maximums of the DQDV curve, and the red dots represent the local minimums.

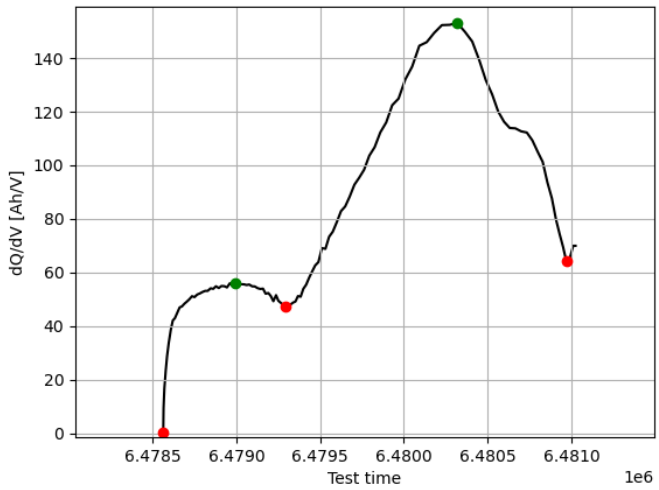

Figure 5.1: DQDV features

The number of local maximums and minimums found depends on the SoC interval used and will therefore differ for the LIBs in this project.

Based on LIB domain knowledge, other features like temperature and data extracted from the CCCV charging phase are used. Table 5.2 lists all the extracted features.

Feature	**Description**
Maximum DQDV value.	Local maximum value from the DQDV discharge curve.
Minimum DQDV value.	Local minimum value from the DQDV discharge curve.
Maximum DQDV time.	Relative timestamp of the local maximum value of the DQDV discharge curve.
Minimum DQDV time	Relative timestamp of the local minimum value of the DQDV discharge curve.
CCCV charging time	The time used to complete CCCV charging phase.
CCCV minimum current	The minimum current used in the CCCV charging phase.
Average temperature	The average temperature during the discharge phase.

Table 5.2: Extracted Features

5.4 Model Training and Validation

Different data sets are needed to tune hyperparameters and validate the models. First, the whole data set is split into two, one data set for hyperparameter tuning and one for validation. The data set selected for hyperparameter tuning was temporally ordered earlier than the data selected for model validation to avoid data leakage. Both the hyperparameter data set and the validation data set are split again into multiple pairs of training and test data sets. To prevent overfitting, the training data is always temporally ordered ahead of the test data. Additionally, the validation data needs to be temporally ordered to relate the LIB aging to the different machine learning model's behavior. In the validation data set, there are 18 or 19 training and testing pairs, depending on from which cell the data is obtained. Only one set is used for tuning hyperparameters. This was deemed sufficient because the goal is to explore the change in accuracy and feature importance under the time series development, not to create the most accurate models. Figure 5.2 illustrates how the data is split into different sets.

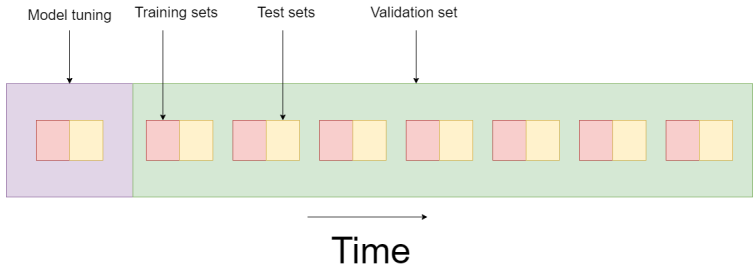

Figure 5.2: Training and validation set split illustration

The performance of the models is evaluated using the model's test data predictions. Since the value of the target changes over time in individual time series and between time series, a scale invariant error metric must be used. Mean Absolute Scaled Error (MASE) is selected as it is scale invariant, penalizes both positive and negative forecast errors, and is easy to interpret. The formula for MASE is:

$$MASE = \frac{\frac{1}{H}\sum_{h}^{H}|e_h|}{\frac{1}{H-1}\sum_{h+1}^{H}|Y_t - Y_{t-1}|} \tag{5.2}$$

H is the horizon of the prediction. $|e_h|$ is the absolute value of the error between the observed value and forecast at time step h. $|Y_t - Y_{t-1}|$ is the absolute error

of the forecast from the naïve forecast method. The simple naïve forecasts are created by setting the forecast equal to the last observed value in the time series. The target of the predictions is the LIB capacity. As explained in subsection 4.2.2, it is clear that the target has a trend. The naïve forecast needs to account for this to be somewhat accurate. Therefore the recent trend is calculated from the last 20 time steps. The calculated trend is then added to the predictions, yielding the formula for a naïve prediction h time steps ahead:

$$Y_{T+h|T} = Y_t + h\frac{Y_t - y_{T-20}}{T-1} \tag{5.3}$$

It is simple to interpret the calculated MASE values. A MASE smaller than 1 indicates that the created model outperformed the naïve method. A MASE greater than 1, indicates that the naïve method made better predictions than our model.

5.5 SHAP Values

After model training, the SHAP for each prediction in the test set is calculated. The SHAP values are estimated using the "shap" python package [Lundberg and Lee, 2017c]. Specifically, the "KernelExplainer" class, which is model agnostic, is used to estimate the SHAP values of both model 1 and model 2.

Chapter 6

Model Analysis

This chapter presents the obtained results from the models and analysis of these results. First, the performance of the models are analyzed to ensure that they have some predictive power. Next the SHAP values of the models with satisfactory performance are analyzed. These can provide insight into which features are important at specific SoC ranges, and if the importance of the features change over time.

6.1 Model Performance

The performance results of the models are evaluated using the MASE metric, as explained in section 5.4. The MASE is calculated for the whole validation set. Next the relationship between the obtained performance results and the degradation of the LIBs is explored.

6.1.1 Performance Results of Model 1

Figure 6.1 plots a typical capacity prediction created by model 1. The prediction is 100 cycles ahead.

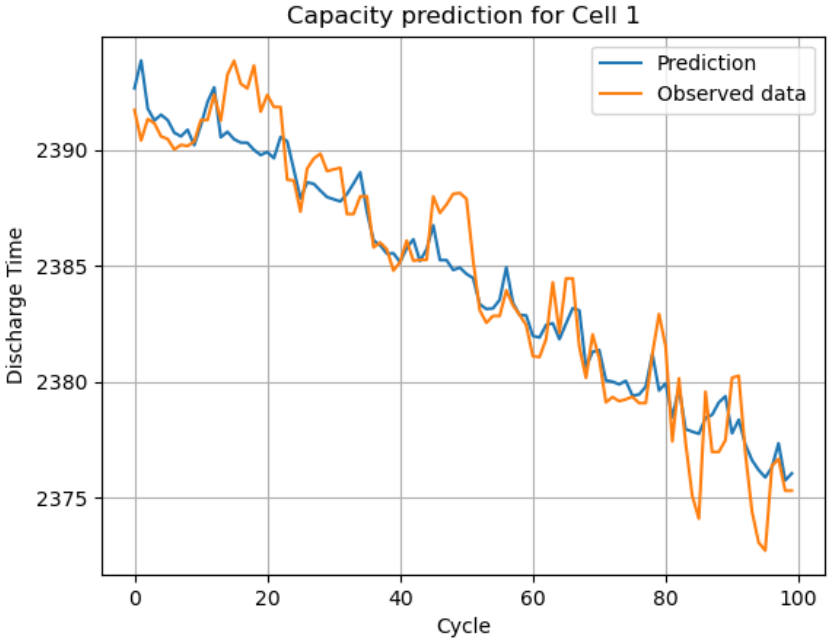

Figure 6.1: Model 1 capacity prediction example

Table 6.1 gives the average MASE of the validation set for model 1 for all 4 cells. We observe that model 1 outperforms the naïve forecasts for every cell. The worst forecasts, according to MASE, is obtained from the forecasts created for cell 1. The validation set of cell 4 gives the next worst MASE. The best and second best MASE is obtained in the validation sets for cell 3 and 4 respectively.

Cell Number	**Model MASE**
1	0.78
2	0.57
3	0.45
4	0.59

Table 6.1: Model 1 average mean absolute scaled error

6.1.2 Performance Results of Model 2

Figure 6.2 plots a 100 step capacity prediction made by model 2.

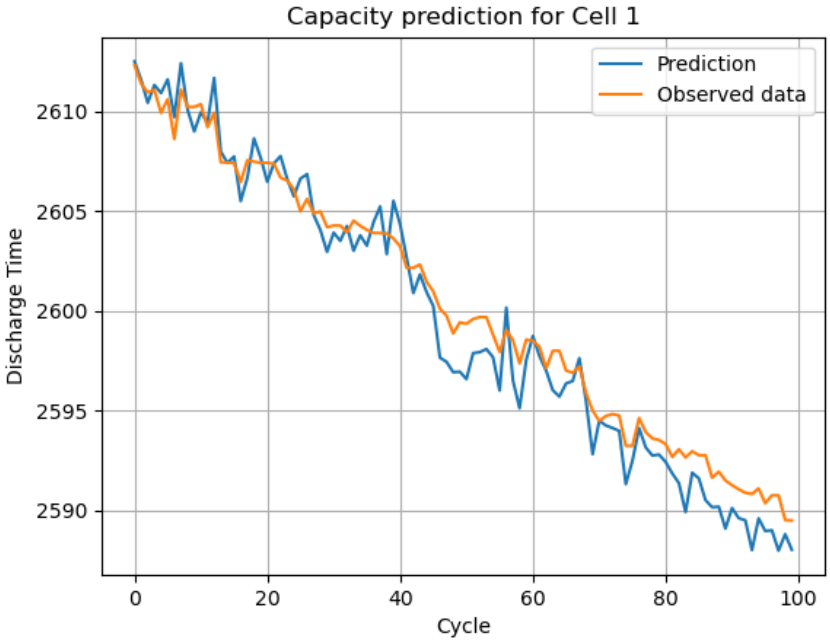

Figure 6.2: Model 2 capacity prediction example

Table 6.2 gives the average MASE of the validation set for model 2 for all 4 cells. Every MASE is below 1 and model 2 outperforms the naïve forecasts for every cell. The validation set of cell 1 gives the worst MASE, cell 4 gives the second worst MASE. The best MASE is obtained when evaluating the forecasts of the capacity of cell 3 and the second best is obtained when evaluating cell 2.

Cell Number	Model MASE
1	0.92
2	0.58
3	0.52
4	0.64

Table 6.2: Model 2 average Mean absolute scaled error

6.1.3 Model Performance and LIB Degradation

Both model 1 and model 2 have the least success in predicting the capacity degradation of cell 1. A possible explanation could be the increased capacity loss of cell 1 when compared to cell 2 and cell 3, as discussed in subsection 4.2.2. On the other hand, the MASE is significantly larger for cell 1 than for cell 4 for both model 1 and model 2, and cell 4 experiences close to the same capacity loss as cell 1. From 4.2.4 it is clear that cell 1 has more LLI and LAM when compared to the three other cells. The explanation to why both model 1 and model 2 have more difficulty in predicting the behavior of cell 1 could be the increased LLI and LAM in cell 1. Faster change in degradation mode could manifest itself as more non-stationary elements in the input features of the models. This could also explain why the MASE for cell 2, cell 3, and cell 4 are comparable, as their degradation modes are also comparable.

6.2 SHAP Results and Discussion

The following subsections list all the calculated estimates of SHAP for all the input features for both model 1 and model 2. A discussion on the obtained SHAP results is also provided. The features from the previous section, 5.3, are renamed in this section in order to fit them in the tables given below. The minimum CCCV charging current is renamed to "current". The time interval spent in CCCV charging mode is named "interval". The DQDV local maximums are sorted in ascending order according to the time they are observed. To illustrate, the first local max DQDV feature is labeled "DQDV 1". Likewise, the feature representing the timestamp of the first local maximum DQDV value is renamed to "Max time 1". The renaming of the local minimums is done in the same way as the local maximums. Lastly, the average temperature feature is renamed to "T". The features are sorted after their importance where the features in column "1" have the greatest importance and the features in the last column have least importance. Each prediction has a horizon of 100 and the average

feature importance of the horizon is listed. For cell 1, 18 sets from the validation set was used to test the feature importance, because of limitations in the amount of data points. For cell 2, cell 3 and cell 4, 19 test were executed.

6.2.1 SHAP for Cell 1

Table 6.3 lists the feature importance for all predictions of model 1 and table 6.4 lists the feature importance in the predictions of model 2. It can be observed that model 1 and model 2 agree on which features are most important in every prediction. In addition, the feature importance does not differ in any of the different predictions, from one to eighteen.

From the 10%-90% SoC window that cell 1 is cycled in, we obtain two local minimum DQDV values and one maximum DQDV value. Since the "Min 1" feature is always sampled at time 0, the "Min time 1" feature is dropped and 8 features remain.

Prediction number	**1**	**2**	**3**	**4**	**5**	**6**	**7**	**8**
1	Current	Interval	Min time 2	Max time 1	Min 2	Min 1	Max 1	T
2	Current	Interval	Min time 2	Max time 1	Min 2	Min 1	Max 1	T
3	Current	Interval	Min time 2	Max time 1	Min 2	Min 1	Max 1	T
4	Current	Interval	Min time 2	Max time 1	Min 2	Min 1	Max 1	T
5	Current	Interval	Min time 2	Max time 1	Min 2	Min 1	Max 1	T
6	Current	Interval	Min time 2	Max time 1	Min 2	Min 1	Max 1	T
7	Current	Interval	Min time 2	Max time 1	Min 2	Min 1	Max 1	T
8	Current	Interval	Min time 2	Max time 1	Min 2	Min 1	Max 1	T
9	Current	Interval	Min time 2	Max time 1	Min 2	Min 1	Max 1	T
10	Current	Interval	Min time 2	Max time 1	Min 2	Min 1	Max 1	T
11	Current	Interval	Min time 2	Max time 1	Min 2	Min 1	Max 1	T
12	Current	Interval	Min time 2	Max time 1	Min 2	Min 1	Max 1	T
13	Current	Interval	Min time 2	Max time 1	Min 2	Min 1	Max 1	T
14	Current	Interval	Min time 2	Max time 1	Min 2	Min 1	Max 1	T
15	Current	Interval	Min time 2	Max time 1	Min 2	Min 1	Max 1	T
16	Current	Interval	Min time 2	Max time 1	Min 2	Min 1	Max 1	T
17	Current	Interval	Min time 2	Max time 1	Min 2	Min 1	Max 1	T
18	Current	Interval	Min time 2	Max time 1	Min 2	Min 1	Max 1	T

Table 6.3: Sorted feature importance for model 1 when predicting data from cell 1

Prediction number	1	2	3	4	5	6	7	8
1	Current	Interval	Min time 2	Max time 1	Min 2	Min 1	Max 1	T
2	Current	Interval	Min time 2	Max time 1	Min 2	Min 1	Max 1	T
3	Current	Interval	Min time 2	Max time 1	Min 2	Min 1	Max 1	T
4	Current	Interval	Min time 2	Max time 1	Min 2	Min 1	Max 1	T
5	Current	Interval	Min time 2	Max time 1	Min 2	Min 1	Max 1	T
6	Current	Interval	Min time 2	Max time 1	Min 2	Min 1	Max 1	T
7	Current	Interval	Min time 2	Max time 1	Min 2	Min 1	Max 1	T
8	Current	Interval	Min time 2	Max time 1	Min 2	Min 1	Max 1	T
9	Current	Interval	Min time 2	Max time 1	Min 2	Min 1	Max 1	T
10	Current	Interval	Min time 2	Max time 1	Min 2	Min 1	Max 1	T
11	Current	Interval	Min time 2	Max time 1	Min 2	Min 1	Max 1	T
12	Current	Interval	Min time 2	Max time 1	Min 2	Min 1	Max 1	T
13	Current	Interval	Min time 2	Max time 1	Min 2	Min 1	Max 1	T
14	Current	Interval	Min time 2	Max time 1	Min 2	Min 1	Max 1	T
15	Current	Interval	Min time 2	Max time 1	Min 2	Min 1	Max 1	T
16	Current	Interval	Min time 2	Max time 1	Min 2	Min 1	Max 1	T
17	Current	Interval	Min time 2	Max time 1	Min 2	Min 1	Max 1	T
18	Current	Interval	Min time 2	Max time 1	Min 2	Min 1	Max 1	T

Table 6.4: Sorted feature importance for model 2 when predicting data from cell 1

6.2.2 SHAP for Cell 2

Table 6.5 gives the feature importance for all predictions of model 1. Table 6.6 lists the average feature importance in the predictions of model 2. For model 1 the feature importance does not change throughout the validation set, except for prediction number five, where "Interval" and "Current" exchange place. The feature importance in model 2 is also mostly constant over all the predictions. There are some exceptions mostly due to "Interval" and "Min time 2" switching place. There are some deviations, but it can be noted that model 1 and model 2 on average mostly agree on which features are most important in nearly all predictions.

Cell 2 is cycled in the 20%-50% SoC window. From this SoC window, two local minimum DQDV values and one maximum DQDV value are obtained. As the "Min 1" is always sampled at time 0, there are 8 features left.

Prediction number	1	2	3	4	5	6	7	8
1	Current	Interval	Min time 2	Max time 1	Min 2	Min 1	Max 1	T
2	Current	Interval	Min time 2	Max time 1	Min 2	Min 1	Max 1	T
3	Current	Interval	Min time 2	Max time 1	Min 2	Min 1	Max 1	T
4	Current	Interval	Min time 2	Max time 1	Min 2	Min 1	Max 1	T
5	Interval	Current	Min time 2	Max time 1	Min 2	Min 1	Max 1	T
6	Current	Interval	Min time 2	Max time 1	Min 2	Min 1	Max 1	T
7	Current	Interval	Min time 2	Max time 1	Min 2	Min 1	Max 1	T
8	Current	Interval	Min time 2	Max time 1	Min 2	Min 1	Max 1	T
9	Current	Interval	Min time 2	Max time 1	Min 2	Min 1	Max 1	T
10	Current	Interval	Min time 2	Max time 1	Min 2	Min 1	Max 1	T
11	Current	Interval	Min time 2	Max time 1	Min 2	Min 1	Max 1	T
12	Current	Interval	Min time 2	Max time 1	Min 2	Min 1	Max 1	T
13	Current	Interval	Min time 2	Max time 1	Min 2	Min 1	Max 1	T
14	Current	Interval	Min time 2	Max time 1	Min 2	Min 1	Max 1	T
15	Current	Interval	Min time 2	Max time 1	Min 2	Min 1	Max 1	T
16	Current	Interval	Min time 2	Max time 1	Min 2	Min 1	Max 1	T
17	Current	Interval	Min time 2	Max time 1	Min 2	Min 1	Max 1	T
18	Current	Interval	Min time 2	Max time 1	Min 2	Min 1	Max 1	T
19	Current	Interval	Min time 2	Max time 1	Min 2	Min 1	Max 1	T

Table 6.5: Sorted feature importance for model 1 when predicting data from cell 2

Prediction number	1	2	3	4	5	6	7	8
1	Current	Interval	Min time 2	Max time 1	Min 2	Min 1	Max 1	T
2	Current	Interval	Min time 2	Max time 1	Min 2	Min 1	Max 1	T
3	Current	Interval	Min time 2	Max time 1	Min 2	Min 1	Max 1	T
4	Current	Interval	Min time 2	Max time 1	Min 2	Min 1	Max 1	T
5	Interval	T	Min 2	Max 1	Min 1	Max time 1	Min time 2	Current
6	Current	Interval	Min time 2	Max time 1	Min 2	Min 1	Max 1	T
7	Current	Interval	Min time 2	Max time 1	Min 2	Min 1	Max 1	T
8	Current	Interval	Min time 2	Max time 1	Min 2	Min 1	Max 1	T
9	Current	Interval	Min time 2	Max time 1	Min 2	Min 1	Max 1	T
10	Current	Min time 2	Interval	Max time 1	Min 2	Min 1	Max 1	T
11	Current	Interval	Min time 2	Max time 1	Min 2	Min 1	Max 1	T
12	Current	Min time 2	Interval	Max time 1	Min 2	Min 1	Max 1	T
13	Current	Interval	Min time 2	Max time 1	Min 2	Min 1	Max 1	T
14	Current	Interval	Min time 2	Max time 1	Min 2	Min 1	Max 1	T
15	Current	Interval	Min time 2	Max time 1	Min 2	Min 1	Max 1	T
16	Current	Interval	Min time 2	Max time 1	Min 2	Min 1	Max 1	T
17	Current	Min time 2	Interval	Max time 1	Min 2	Min 1	Max 1	T
18	Current	Min time 2	Interval	Max time 1	Min 2	Min 1	Max 1	T
19	Current	Interval	Min time 2	Max time 1	Min 2	Min 1	Max 1	T

Table 6.6: Sorted feature importance for model 2 when predicting data from cell 2

6.2.3 SHAP for Cell 3

Table 6.7 gives the feature importance for all predictions of model 1 and table 6.8 gives the importance of the features in model 2. For model 1, there are many fluctuations in the feature importance. "Current", "Interval" and "Max time 1" are often listed as important, while "T", "Max 1" and "Min 1" are frequently listed as less important. There is no obvious pattern developing throughout the series of predictions, meaning there is no feature that consistently gains or losses importance. By inspecting table 6.8, it can be observed that the importance of the features also fluctuate in model 2. Generally, the features "Current, "T" and "Max time 1" are often given high importance while the features "Interval", "Max 1" and "Min 1" are attributed less importance. Likewise as for model 1, there is no clear pattern where any feature climbs or sinks in importance over time.

The SoC window of cell 3, is 35%-65%. From this SoC window, one minimum DQDV value and one maximum DQDV value are obtained. As the "Min 1" is always sampled at time 0, there are only 6 features left.

Prediction number	**1**	**2**	**3**	**4**	**5**	**6**
1	Interval	T	Max 1	Current	Max time 1	Min 1
2	Current	Max time 1	Interval	Min 1	Max 1	T
3	Current	Interval	Max time 1	Min 1	T	Max 1
4	Current	Interval	T	Max time 1	Min 1	Max 1
5	Interval	T	Current	Max 1	Max time 1	Min 1
6	Current	Interval	Max time 1	T	Min 1	Max 1
7	Current	Max time 1	Min 1	Interval	Max 1	T
8	Current	Interval	Max time 1	Min 1	T	Max 1
9	Current	Max time 1	Min 1	Interval	Max 1	T
10	Current	Interval	Max time 1	Min 1	T	Max 1
11	Interval	T	Current	Max time 1	Max 1	Min 1
12	Interval	Current	T	Max time 1	Max 1	Min 1
13	Current	Max time 1	Min 1	Interval	Max 1	T
14	Interval	T	Current	Max time 1	Max 1	Min 1
15	Interval	T	Current	Max time 1	Min 1	Max 1
16	Current	Max time 1	Min 1	Interval	Max 1	T
17	Current	Max time 1	Min 1	Interval	Max 1	T
18	Current	Interval	Max time 1	Min 1	Max 1	T
19	Interval	Current	T	Max time 1	Min 1	Max 1

Table 6.7: Sorted feature importance for model 1 when predicting data from cell 3

Prediction number	1	2	3	4	5	6
1	T	Max 1	Min 1	Max time 1	Current	Interval
2	Current	Max time 1	Min 1	Max 1	Interval	T
3	Current	Max time 1	Min 1	Interval	Max 1	T
4	Current	Max time 1	Min 1	T	Interval	Max 1
5	Current	Max time 1	Interval	Min 1	Max 1	T
6	T	Max 1	Max time 1	Interval	Min 1	Current
7	Current	Max time 1	Min 1	Interval	Max 1	T
8	T	Max 1	Current	Interval	Max time 1	Min 1
9	Current	Max time 1	Min 1	Interval	Max 1	T
10	Current	T	Max 1	Min time 1	Interval	Min 1
11	Current	T	Max time 1	Min 1	Interval	Max 1
12	Current	T	Max time 1	Min 1	Max 1	Interval
13	Current	Max time 1	Min 1	Interval	Max 1	T
14	Current	T	Max time 1	Interval	Min 1	Max 1
15	Current	Max time 1	Min 1	Interval	Max 1	T
16	Current	Max time 1	Interval	T	Min 1	Max 1
17	T	Max time 1	Max 1	Interval	Current	Min 1
18	Current	Max time 1	Interval	Min 1	T	Max 1
19	Current	T	Max time 1	Interval	Min 1	Max 1

Table 6.8: Sorted feature importance for model 2 when predicting data from cell 3

6.2.4 SHAP for Cell 4

The feature importance of model 1 is given in table 6.9 and table 6.10 lists the importance of the features in model 2. There are many variations in the feature importance for model 1. However "T", "Interval" and "Max 1" are frequently listed as important, while "Max time 1", "Min time 1", "Current", and "Min 1" are frequently listed as less important. It is not easy to distinguish any clear trends where a feature gains or looses importance over time. By inspecting table 6.10, it is clear that the importance of the features also fluctuate in model 2. The features "T, "Interval" and "Min 1" are often attributed high importance while the features "Max time 1", "Min time 1", "Current" and "Max 1" are given less importance. There is no clear pattern where any feature importance increases or decreases over time for model 2.

The SoC window of cell 4, is 65%-95%. From this SoC window, one minimum DQDV value and one maximum DQDV value are obtained. This yields a total of 6 features.

Prediction number	1	2	3	4	5	6	7
1	T	Interval	Max 1	Max time 1	Min 1	Current	Min time 1
2	Interval	T	Min 1	Current	Max 1	Max time 1	Min time 1
3	T	Max 1	Current	Min 1	Min time 1	Max time 1	Interval
4	T	Interval	Current	Min time 1	Min 1	Max 1	Max time 1
5	T	Interval	Min time 1	Current	Min 1	Max time 1	Max 1
6	T	Interval	Max time 1	Max 1	Current	Min time 1	Min 1
7	Min 1	Interval	Min time 1	T	Max time 1	Current	Max 1
8	T	Interval	Current	Min time 1	Min 1	Max time 1	Max 1
9	T	Current	Min time 1	Max 1	Max time 1	Min 1	Interval
10	T	Interval	Max time 1	Min 1	Min time 1	Max 1	current
11	Interval	Max 1	T	Current	Min 1	Max time 1	Min time 1
12	T	Min 1	Max 1	Max time 1	Min time 1	Interval	Current
13	Interval	T	Max 1	Min 1	Current	Max time 1	Min time 1
14	T	Interval	Max 1	Min 1	Min time 1	Current	Max time 1
15	Interval	Min 1	T	Min time 1	Max 1	Max time 1	Current
16	T	Max 1	Min time 1	Current	Min 1	Interval	Max time 1
17	T	Max time 1	Current	Interval	Min 1	Min time 1	Max 1
18	Min time 2	Interval	Max time 1	Min 2	Min 1	Max 1	T
19	T	Interval	Min time 1	Min time 1	Min 1	Max 1	Current

Table 6.9: Sorted feature importance for model 1 when predicting data from cell 4

Prediction number	1	2	3	4	5	6	7
1	Min 1	Interval	T	Min time 1	Current	Max time 1	Max 1
2	T	Interval	Min 1	Current	Max time 1	Max 1	Min time 1
3	Interval	Min 1	T	Current	Max time 1	Max 1	Min time 1
4	Min 1	Interval	Max 1	Current	Max time 1	Min time 1	T
5	Interval	T	Min 1	Max 1	Max time 1	Min time 1	Current
6	Interval	Min 1	T	Max 1	Current	Min time 1	Max time 1
7	Min 1	T	Interval	Current	Min time 1	Max time 1	Max 1
8	Min 1	Interval	Max time 1	Min time 1	Max 1	T	Current
9	T	Min 1	Interval	Max time 1	Max 1	Min time 1	Current
10	T	Interval	Max 1	Current	Min 1	Min time 1	Max time 1
11	T	Interval	Max 1	Current	Max time 1	Min 1	Min time 1
12	T	Min 1	Interval	Min time 1	Max time 1	Current	Max 1
13	Interval	Min 1	Max time 1	Max 1	Min time 1	T	Current
14	T	Min 1	Interval	Max 1	Max time 1	Min time 1	Current
15	Min 1	T	Interval	Max 1	Current	Min time 1	Max time 1
16	Interval	T	Min 1	Current	Max 1	Min time 1	Max time 1
17	T	Interval	Max time 1	Min 1	Max 1	Current	Min time 1
18	T	Interval	Max time 1	Min 1	Max 1	Current	Min time 1
19	T	Interval	Min 1	Max time 1	Min time 1	Current	Max 1

Table 6.10: Sorted feature importance for model 2 when predicting data from cell 4

6.2.5 SHAP Relation to LIB Degradation and SoC Windows

By observing the feature importance of cell 1, which is the cell that ages the most, it is clear that the feature importance is constant for the duration of the project for both model 1 and model 2. By inspecting the importance of the input features of cell 2, cell 3, and cell 4, there is no clear trends where any feature gains or looses importance in both model 1 and mode 2. These results indicate that the feature importance does not change, at least in the machine learning models used in this thesis, due to the LIBs aging, in any significant way.

The SoC window the LIBs are cycled in, impacts which features are extracted from the DQDV curve. How the number of input features affects the model accuracy is difficult to answer using the obtained data. Intuitively one would think that more information would result in better performing models. But the models predicting the capacity of cell 3, which has only 6 input features, are the best performing models with the lowest MASE. In "Data-driven prediction of battery cycle life before capacity degradation" [Severson et al., 2019], three models predicting capacity degradation was compared. The models differ in the number of input features. The results indicate, although the prediction error decreased with increasing number of features, that selecting the correct features are more important than selecting a large number of features. This explanation seems to be consistent with the results obtained in this thesis. It is difficult to infer anything about which features are most important in the different SoC windows by inspecting the SHAP. Especially since model 1 and model 2 do not completely agree in feature importance when predicting the capacities of cell 3 and cell 4. In general it seems like the features, "Current" and "Interval" which are extracted from the CCCV phase are powerful predictors, in all SoC windows.

Chapter 7

Conclusion and Future Work

This chapter explains the work conducted to attempt to achieve the goal of the thesis as defined in section 1.2. A discussion on the obtained results and how they can answer the research questions is provided. Next, the limitations of the work is discussed, the contributions are listed and suggestions for future extensions of the work are made.

7.1 Conclusion

As stated in section 1.2, this thesis aims to provide a better understanding of the effect of the SoC window on machine learning models for estimation of the SoH in LIBs. To achieve this, a special data set of LIBs cycled in specific SoC windows was created. The data was analyzed to highlight the differences in aging caused by the distinct SoC windows. Two models capable of predicting SoH parameters using the created data set were made. Both model's predictive power was analyzed and the SHAP of the respective input features of both models were calculated and compared. The discussion illustrated that cell 1, which is the cell with the largest SoC cycle window and, as expected according to [Wikner, 2019], experienced the most aging, also gave a larger prediction MASE when compared to the cells cycled at smaller SoC windows. This result can help answer research question one as defined in section 1.2: *"How does data from a LIB cycled at a specific SoC window affect the accuracy of SoH estimates?"* More data is needed and more machine learning methods need to be tested on the data to conclude, but the results in this thesis indicate that the increased degradation of cells cycled in large SoC windows decreases the estimation accuracy of SoH for machine learning methods. Next an attempt was made to answer research question two, defined in section 1.2: *"Which features are most important for estimating the*

SoH and does the SoC window impact feature importance?" The SHAP of both model's predictions were calculated and analyzed from the start of the LIB aging to the end. From the discussion it is clear that the results did not indicate that the importance of features increased or decreased depending on the different SoC windows. Which features are important in the different SoC ranges was also difficult to answer from the analysis. In conclusion more data is needed to infer anything meaningful on research question 2.

7.2 Limitations

The main limitation in the conducted work was the amount of obtained data. To conclude anything with certainty more cells must be tested. In addition, more machine learning models must be created and tested. Due to limited time, the LIBs used in this thesis were not aged to their end of life. Therefore, by increasing the time frame of the project, other interesting relations between SoC and machine learning SoH estimation could be found. Unfortunately, a lot of internal resistance data was rendered useless because of measurement difficulty. The internal resistance of a LIB is important in SoH characterization. Unfortunately this dimension was lost in this project. Another, more general problem, is that there is no obvious and common agreed upon way to define SoH. Therefore, different work will have different definitions of SoH. This makes reasoning about the research questions in this thesis more challenging.

7.3 Contributions

1. *Two machine learning models capable of predicting capacity degradation of LIBs.*
2. *A methodology for creating data which can be used to study SoC impact on machine learning estimation of SoH in LIBs.*
3. *A data set which can be used to study SoC impact on machine learning estimation of SoH in LIBs.*
4. *Indications that increased degradation caused by large SoC windows impact SoH estimation accuracy in machine learning models.*

7.4 Future Work

To increase the certainty of the results in this thesis, the number of tested LIBs in all SoC windows, should be increased. To further increase the generality of the

results, more models should be created, tested and compared. In addition, more effort should be put into increasing the accuracy of the models. Due to limited time, this was not a first priority in this work. Moreover, the data used in this thesis differ from data that a realistic use case, like an electric vehicle, would create. An interesting task could be to alter the aging methodology to closer mimic real world examples, while still containing monthly SoH characterizations.

Chapter 8

Appendices

Appendix A

Literature Review

	Synonym 1	Synonym 2	Synonym 3	Synonym 4
Term 1	State of Health	SoH	-	-
Term 2	Battery	Cell	Accumulator	-
Term 3	Estimation	Regression	Approximation	-
Term 4	SoC range	Cycle range	Range	Interval

Table A.1: Key search terms

Criteria	**Description**
IC 1	The study is concerned with $\mathcal{P}$.
IC 2	$\mathcal{S}$ is constrained by $\mathcal{C}$.
IC 3	The study provides an $\mathcal{S}$ and an evaluation of how $\mathcal{S}$ performs.

Table A.2: Inclusion criteria

$\mathcal{P}$	Estimation of the SoH of any battery cell
$\mathcal{C}$	A limited SoC range should be used in solving $\mathcal{P}$
$\mathcal{S}$	A machine learning method should be used in SoH estimation.

Table A.3: Problem, constraint and solution definitions

Search Engine	**Results reviewed**
Scopus	Every result
IEEE Xplore	Every result
CiteSeerX	Every result
ScienceDirect	First 100 results

Table A.4: Search Engines

Paper title	Search engine	Search term	Criteria	Score
Performance mutation mechanism and parametric characterization method of high-capacity lithium-ion battery.	Scopus	T1 ∧ T2 ∧ T3 ∧ T4	IC 1 ∧ IC 2	2
How the utilised SOC window in commercial Li-ion pouch cells influence battery ageing.	Scopus	T1 ∧ T2 ∧ T3 ∧ T4	IC 1 ∧ IC 2	2
Investigation of capacity fade for 18650-type lithium-ion batteries cycled in different state of charge (SoC) ranges.	Scopus	T1 ∧ T2 ∧ T3 ∧ T4	IC 1 ∧ IC 2	2
Multi-Level Model Reduction and Data-Driven Identification of the Lithium-Ion Battery.	Scopus	T1 ∧ T2 ∧ T3 ∧ T4	IC 1 ∧ IC 2	2
Combining machine learning algorithms and an incremental capacity analysis on 18650 cell under different cycling temperature and SOC range.	Scopus	T1 ∧ T2 ∧ T3 ∧ T4	IC 1 ∧ IC 2 ∧ IC 3	3
A Fast Online State of Health Estimation Method for Lithium-Ion Batteries Based on Incremental Capacity Analysis.	Scopus	T1 ∧ T2 ∧ T3 ∧ T4	IC 1 ∧ IC 2 ∧ IC 3	3
Effect of State of Charge Constraints on Fuel Economy and Battery Aging when Using the Equivalent Consumption Minimization Strategy.	Scopus	T1 ∧ T2 ∧ T3 ∧ T4	IC 1 ∧ IC 2	2
Performance mutation mechanism and parametric characterization method of high-capacity lithium-ion battery	Scopus	T1 ∧ T2 ∧ T3 ∧ T4	IC 1	1
Investigation on Cell Performance and Inconsistency Evolution of Series and Parallel Lithium-Ion Battery Modules	Scopus	T1 ∧ T2 ∧ T3 ∧ T4	IC 1	1
Research on Capacity Difference Identification Method of Lithium-ion Battery Pack	Scopus	T1 ∧ T2 ∧ T3 ∧ T4	IC 1	1
Multi-Level Model Reduction and Data-Driven Identification of the Lithium-Ion Battery	Scopus	T1 ∧ T2 ∧ T3 ∧ T4	IC 1 ∧ IC 2	2
Leveraging cell expansion sensing in state of charge estimation: Practical considerations	Scopus	T1 ∧ T2 ∧ T3 ∧ T4		0
Parameter sensitivity analysis and simplification of equivalent circuit model for the state of charge of lithium-ion batteries.	Scopus	T1 ∧ T2 ∧ T3 ∧ T4	IC 1	1
Available discharge capacity estimation according to crate variation of second-used battery.	Scopus	T1 ∧ T2 ∧ T3 ∧ T4	IC 1	1
Long short term memory-based state-of-health prediction algorithm of a rechargeable lithium-ion battery for electric vehicle.	Scopus	T1 ∧ T2 ∧ T3 ∧ T4	IC 1	1
Using SoC online correction method based on parameter identification to optimize the operation range of NI-MH battery for electric boat.	Scopus	T1 ∧ T2 ∧ T3 ∧ T4		0
State of health of lithium ion battery estimation based on charging process.	IEEE Xplore	T1 ∧ T2 ∧ T3 ∧ T4	IC 1 ∧ IC 2	2
Novel method to Estimate SoH of Lithium-Ion Batteries.	IEEE Xplore	T1 ∧ T2 ∧ T3 ∧ T4	IC 1	1
A Flexible State-of-Health Prediction Scheme for Lithium-Ion Battery Packs With Long Short-Term Memory Network and Transfer Learning.	IEEE Xplore	T1 ∧ T2 ∧ T3 ∧ T4	IC 1 ∧ IC 3	2

Paper title	Search engine	Search term	Criteria	Score
Development of Fast SoH Estimation of Li-Ion Battery Pack/Modules Using Multi Series-Parallel based ANN Structure.	IEEE Xplore	T1 ∧ T2 ∧ T3 ∧ T4	IC 1 ∧ IC 3	2
Online State-of-Health Estimation for Li-Ion Battery Using Partial Charging Segment Based on Support Vector Machine.	IEEE Xplore	T1 ∧ T2 ∧ T3 ∧ T4	IC 1 ∧ IC 2 ∧ IC 3	3
A Hierarchical and Flexible Data-Driven Method for Online State-of-Health Estimation of Li-Ion Battery.	IEEE Xplore	T1 ∧ T2 ∧ T3 ∧ T4	IC 1 ∧ IC 3	2
State-of-Health Estimation and Remaining-Useful-Life Prediction for Lithium-Ion Battery Using a Hybrid Data-Driven Method.	IEEE Xplore	T1 ∧ T2 ∧ T3 ∧ T4	IC 1 ∧ IC 3	2
An Ensemble Learning-Based Data-Driven Method for Online State-of-Health Estimation of Lithium-Ion Batteries.	IEEE Xplore	T1 ∧ T2 ∧ T3 ∧ T4	IC 1 ∧ IC 3	2
Charge analysis for Li-ion battery pack state of health estimation for electric and hybrid vehicles.	IEEE Xplore	T1 ∧ T2 ∧ T3 ∧ T4	IC 1	1
A multiscale data-driven framework for lithium-ion battery on-line state estimation.	IEEE Xplore	T1 ∧ T2 ∧ T3 ∧ T4	IC 1 ∧ IC 2	2
Estimation Error Bound of Battery Electrode Parameters With Limited Data Window.	IEEE Xplore	T1 ∧ T2 ∧ T3 ∧ T4	IC 1 ∧ IC 2 ∧ IC 3	3
Fuzzy logic estimation of SOH of 125Ah VRLA batteries.	IEEE Xplore	T1 ∧ T2 ∧ T3 ∧ T4	IC 1 ∧ IC 3	2
Model-Based Lithium-Ion Battery Resistance Estimation From Electric Vehicle Operating Data.	IEEE Xplore	T1 ∧ T2 ∧ T3 ∧ T4	IC 1	1
Solving Limited Data Challenges in Battery Parameter Estimators by Using Generative Adversarial Networks.	IEEE Xplore	T1 ∧ T2 ∧ T3 ∧ T4		0
An adaptive battery capacity estimation method suitable for random charging voltage range in electric vehicles.	IEEE Xplore	T1 ∧ T2 ∧ T3 ∧ T4		0
A Novel Big Data Modeling Method for Improving Driving Range Estimation of EVs.	IEEE Xplore	T1 ∧ T2 ∧ T3 ∧ T4		0
Lithium-ion Battery State of Health Monitoring Based on Ensemble Learning.	IEEE Xplore	T1 ∧ T2 ∧ T3 ∧ T4	IC 1 ∧ IC 3	2
State of Health Estimation of Lithium-Ion Batteries Based on Fixed Size LS-SVM.	IEEE Xplore	T1 ∧ T2 ∧ T3 ∧ T4	IC 1 ∧ IC 2 ∧ IC 3	3
Battery aging estimation for eco-driving strategy and electric vehicles sustainability.	IEEE Xplore	T1 ∧ T2 ∧ T3 ∧ T4	IC 1	1
Fuzzy logic-based state-of-health determination of lead acid batteries.	IEEE Xplore	T1 ∧ T2 ∧ T3 ∧ T4	IC 1	1
Online Data-based Cell State Estimation of a Lithium-Ion Battery.	IEEE Xplore	T1 ∧ T2 ∧ T3 ∧ T4		0

Paper title	Search engine	Search term	Criteria	Score
Online Li-ion battery state of health implementation for grid-tied applications.	IEEE Xplore	T1 ∧ T2 ∧ T3 ∧ T4		0
Self-learning state-of-available-power prediction for lithium-ion batteries in electrical vehicles.	IEEE Xplore	T1 ∧ T2 ∧ T3 ∧ T4	IC 1	1
On-line parameter, state-of-charge and aging estimation of Li-ion batteries.	IEEE Xplore	T1 ∧ T2 ∧ T3 ∧ T4		0
Diagnosis of Electric Vehicle Batteries Using Recurrent Neural Networks.	IEEE Xplore	T1 ∧ T2 ∧ T3 ∧ T4	IC 1 ∧ IC 3	2
Prognostics of remaining useful life for lithium-ion batteries based on a feature vector selection and relevance vector machine approach.	IEEE Xplore	T1 ∧ T2 ∧ T3 ∧ T4	IC 1 ∧ IC 3	2
Health monitoring and remaining useful life estimation of lithium-ion aeronautical batteries.	IEEE Xplore	T1 ∧ T2 ∧ T3 ∧ T4	IC 1	1
Diagnosis of Performance Degradation for Lithium-Ion Battery Module in Electric Vehicle.	IEEE Xplore	T1 ∧ T2 ∧ T3 ∧ T4	IC 1	1
On-line measurement of battery impedance using motor controller excitation.	CiteSeerX	T1 ∧ T2 ∧ T3 ∧ T4		0
Article On-Board State-of-Health Estimation at a Wide Ambient Temperature Range in Lithium-Ion Batteries.	CiteSeerX	T1 ∧ T2 ∧ T3 ∧ T4	IC 1	1
Fuzzy LogicBased State-of-Health Determination.	CiteSeerX	T1 ∧ T2 ∧ T3 ∧ T4	IC 1 ∧ IC 3	2
Electrochemical-based Battery SOC/SOH Estimation.	CiteSeerX	T1 ∧ T2 ∧ T3 ∧ T4		0
State-of-health estimation for lithium-ion batteries by combining model-based incremental capacity analysis with support vector regression.	ScienceDirect	T1 ∧ T2 ∧ T3 ∧ T4	IC 1 ∧ IC 3	2
A multi-feature-based multi-model fusion method for state of health estimation of lithium-ion batteries	ScienceDirect	T1 ∧ T2 ∧ T3 ∧ T4	IC 1 ∧ IC 3	2
Online state-of-health estimation of lithium-ion battery based on dynamic parameter identification at multi timescale and support vector regression.	ScienceDirect	T1 ∧ T2 ∧ T3 ∧ T4	IC 1 ∧ IC 3	2
Machine learning in state of health and remaining useful life estimation: Theoretical and technological development in battery degradation modelling.	ScienceDirect	T1 ∧ T2 ∧ T3 ∧ T4	IC 1 ∧ IC 3	2
A data-fusion framework for lithium battery health condition Estimation Based on differential thermal voltammetry.	ScienceDirect	T1 ∧ T2 ∧ T3 ∧ T4	IC 1	1

Paper title	Search engine	Search term	Criteria	Score
State of health estimation of lithium-ion battery in wide temperature range via temperature-aging coupling mechanism analysis.	ScienceDirect	T1 ∧ T2 ∧ T3 ∧ T4	IC 1	1
Efficient linear predictive model with short term features for lithium-ion batteries state of health estimation.	ScienceDirect	T1 ∧ T2 ∧ T3 ∧ T4	IC 1 ∧ IC 3	2
State of health estimation for Li-ion battery via partial incremental capacity analysis based on support vector regression.	ScienceDirect	T1 ∧ T2 ∧ T3 ∧ T4	IC 1 ∧ IC 3	2
Sparse data machine learning for battery health estimation and optimal design incorporating material characteristics.	ScienceDirect	T1 ∧ T2 ∧ T3 ∧ T4	IC 1 ∧ IC 3	2
Online estimation of battery model parameters and state of health in electric and hybrid aircraft application.	ScienceDirect	T1 ∧ T2 ∧ T3 ∧ T4	IC 1	1
A flexible method for state-of-health estimation of lithium battery energy storage system.	ScienceDirect	T1 ∧ T2 ∧ T3 ∧ T4	IC 1	1
A health indicator extraction and optimization for capacity estimation of Li-ion battery using incremental capacity curves.	ScienceDirect	T1 ∧ T2 ∧ T3 ∧ T4	IC 1 ∧ IC 3	2
State of health estimation of lithium-ion batteries based on the regional frequency.	ScienceDirect	T1 ∧ T2 ∧ T3 ∧ T4	IC 1	1
On-line state-of-health estimation of Lithium-ion battery cells using frequency excitation.	ScienceDirect	T1 ∧ T2 ∧ T3 ∧ T4	IC 1	1
A state-of-health estimation method of lithium-ion batteries based on multi-feature extracted from constant current charging curve.	ScienceDirect	T1 ∧ T2 ∧ T3 ∧ T4	IC 1 ∧ IC 2 ∧ IC 3	3
State of health estimation for lithium-ion battery based on the coupling-loop nonlinear autoregressive with exogenous inputs neural network	ScienceDirect	T1 ∧ T2 ∧ T3 ∧ T4	IC 1 ∧ IC 3	2
State-of-health estimation of batteries in an energy storage system based on the actual operating parameters.	ScienceDirect	T1 ∧ T2 ∧ T3 ∧ T4	IC 1	1
An end-to-end neural network framework for state-of-health estimation and remaining useful life prediction of electric vehicle lithium batteries.	ScienceDirect	T1 ∧ T2 ∧ T3 ∧ T4	IC 1 ∧ IC 3	2
On the feature selection for battery state of health estimation based on charging-discharging profiles.	ScienceDirect	T1 ∧ T2 ∧ T3 ∧ T4	IC 1 ∧ IC 3	2

Paper title	**Search engine**	**Search term**	**Criteria**	**Score**
State of health estimation of lithium-ion battery based on an adaptive tunable of lithium-ion battery using charging curve.	ScienceDirect	T1 ∧ T2 ∧ T3 ∧ T4	IC 1 ∧ IC 3	2
An optimized ensemble learning framework for lithium-ion Battery State of Health estimation in energy storage system.	ScienceDirect	T1 ∧ T2 ∧ T3 ∧ T4	IC 1 ∧ IC 3	2
State-of-health estimation of lithium-ion batteries based on semi-supervised transfer component analysis.	ScienceDirect	T1 ∧ T2 ∧ T3 ∧ T4	IC 1 ∧ IC 3	2
Lithium-ion battery state of health estimation using the incremental capacity and wavelet neural networks with genetic algorithm.	ScienceDirect	T1 ∧ T2 ∧ T3 ∧ T4	IC 1 ∧ IC 3	2
A novel deep learning framework for state of health estimation of lithium-ion battery.	ScienceDirect	T1 ∧ T2 ∧ T3 ∧ T4	IC 1 ∧ IC 3	2
A uniform estimation framework for state of health of lithium-ion batteries considering feature extraction and parameters optimization.	ScienceDirect	T1 ∧ T2 ∧ T3 ∧ T4	IC 1 ∧ IC 3	2
Small sample state of health estimation based on weighted Gaussian process regression.	ScienceDirect	T1 ∧ T2 ∧ T3 ∧ T4	IC 1 ∧ IC 3	2
A novel Gaussian process regression model for state-of-health estimation hybrid radial basis function network.	ScienceDirect	T1 ∧ T2 ∧ T3 ∧ T4	IC 1 ∧ IC 3	2
State-of-health estimation and remaining useful life prediction for the lithium-ion battery based on a variant long short term memory neural network.	ScienceDirect	T1 ∧ T2 ∧ T3 ∧ T4	IC 1 ∧ IC 3	2
A partial charging curve-based data-fusion-model method for capacity estimation of Li-Ion battery.	ScienceDirect	T1 ∧ T2 ∧ T3 ∧ T4	IC 1 ∧ IC 3	2
State of health forecasting of Lithium-ion batteries applicable in real-world operational conditions.	ScienceDirect	T1 ∧ T2 ∧ T3 ∧ T4	IC 1 ∧ IC 3	2

Table A.5: Reviewed papers

Bibliography

Awad, M. and Khanna, R. (2015). *Support Vector Regression*, pages 67–80.

Birkl, C. R., Roberts, M. R., McTurk, E., Bruce, P. G., and Howey, D. A. (2017). Degradation diagnostics for lithium ion cells. *Journal of Power Sources*, 341:373–386.

Burheim, O. S. (2017). *Engineering energy storage*. Academic press.

Chen, Z., Xia, X., Sun, M., Shen, J., and Xiao, R. (2018). State of health estimation of lithium-ion batteries based on fixed size ls-svm. In *2018 IEEE Vehicle Power and Propulsion Conference (VPPC)*, pages 1–6. IEEE.

Dubarry, M., Truchot, C., and Liaw, B. Y. (2012). Synthesize battery degradation modes via a diagnostic and prognostic model. *Journal of power sources*, 219:204–216.

Feng, X., Weng, C., He, X., Han, X., Lu, L., Ren, D., and Ouyang, M. (2019). Online state-of-health estimation for li-ion battery using partial charging segment based on support vector machine. *IEEE Transactions on Vehicular Technology*, 68(9):8583–8592.

Gao, Y., Jiang, J., Zhang, C., Zhang, W., and Jiang, Y. (2018). Aging mechanisms under different state-of-charge ranges and the multi-indicators system of state-of-health for lithium-ion battery with li (nimnco) o2 cathode. *Journal of Power Sources*, 400:641–651.

Grytten, H. (2021). Research Plan. *TDT39 Empirical studies in IT, NTNU*.

Guo, Y., Huang, K., and Hu, X. (2021). A state-of-health estimation method of lithium-ion batteries based on multi-feature extracted from constant current charging curve. *Journal of Energy Storage*, 36:102372.

Hyndman, R. J. and Athanasopoulos, G. (2018). *Forecasting: principles and practice*. OTexts.

Keil, P. and Jossen, A. (2016). Calendar aging of nca lithium-ion batteries investigated by differential voltage analysis and coulomb tracking. *Journal of The Electrochemical Society*, 164(1):A6066.

Krupp, A., Ferg, E., Schuldt, F., Derendorf, K., and Agert, C. (2020). Incremental capacity analysis as a state of health estimation method for lithium-ion battery modules with series-connected cells. *Batteries*, 7(1):2.

Lai, J., Chao, D., Wu, A., and Wang, C. (2020). Combining machine learning algorithms and an incremental capacity analysis on 18650 cell under different cycling temperature and soc range. In *E3S Web of Conferences*, volume 182, page 03007. EDP Sciences.

Lee, S., Mohtat, P., Siegel, J. B., Stefanopoulou, A. G., Lee, J.-W., and Lee, T.-K. (2019). Estimation error bound of battery electrode parameters with limited data window. *IEEE Transactions on Industrial Informatics*, 16(5):3376–3386.

Li, P., Zhang, Z., Xiong, Q., Ding, B., Hou, J., Luo, D., Rong, Y., and Li, S. (2020). State-of-health estimation and remaining useful life prediction for the lithium-ion battery based on a variant long short term memory neural network. *Journal of power sources*, 459:228069.

Lundberg, S. M. and Lee, S.-I. (2017a). Consistent feature attribution for tree ensembles. *arXiv preprint arXiv:1706.06060*.

Lundberg, S. M. and Lee, S.-I. (2017b). A unified approach to interpreting model predictions. In *Proceedings of the 31st international conference on neural information processing systems*, pages 4768–4777.

Lundberg, S. M. and Lee, S.-I. (2017c). A unified approach to interpreting model predictions. In Guyon, I., Luxburg, U. V., Bengio, S., Wallach, H., Fergus, R., Vishwanathan, S., and Garnett, R., editors, *Advances in Neural Information Processing Systems*, volume 30. Curran Associates, Inc.

Mitchell, T. (1997). *Machine Learning*. IL McGraw Hill.

Murbach, M. D., Gerwe, B., Dawson-Elli, N., and kun Tsui, L. (2020). impedance.py: A python package for electrochemical impedance analysis. *Journal of Open Source Software*, 5(52):2349.

Noura, N., Boulon, L., and Jemeï, S. (2020). A review of battery state of health estimation methods: Hybrid electric vehicle challenges. *World Electric Vehicle Journal*, 11(4):66.

Pastor-Fernández, C., Uddin, K., Chouchelamane, G. H., Widanage, W. D., and Marco, J. (2017). A comparison between electrochemical impedance spectroscopy and incremental capacity-differential voltage as li-ion diagnostic techniques to identify and quantify the effects of degradation modes within battery management systems. *Journal of Power Sources*, 360:301–318.

Pedregosa, F., Varoquaux, G., Gramfort, A., Michel, V., Thirion, B., Grisel, O., Blondel, M., Prettenhofer, P., Weiss, R., Dubourg, V., Vanderplas, J., Passos, A., Cournapeau, D., Brucher, M., Perrot, M., and Duchesnay, E. (2011). Scikit-learn: Machine learning in Python. *Journal of Machine Learning Research*, 12:2825–2830.

Pinson, M. B. and Bazant, M. Z. (2012). Theory of sei formation in rechargeable batteries: capacity fade, accelerated aging and lifetime prediction. *Journal of the Electrochemical Society*, 160(2):A243.

Prokhorenkova, L., Gusev, G., Vorobev, A., Dorogush, A. V., and Gulin, A. (2018). Catboost: unbiased boosting with categorical features. *Advances in neural information processing systems*, 31.

Qu, S., Kang, Y., Gu, P., Zhang, C., and Duan, B. (2019). A fast online state of health estimation method for lithium-ion batteries based on incremental capacity analysis. *Energies*, 12(17):3333.

Roy, P. and Srivastava, S. K. (2015). Nanostructured anode materials for lithium ion batteries. *Journal of Materials Chemistry A*, 3(6):2454–2484.

Severson, K. A., Attia, P. M., Jin, N., Perkins, N., Jiang, B., Yang, Z., Chen, M. H., Aykol, M., Herring, P. K., Fraggedakis, D., et al. (2019). Data-driven prediction of battery cycle life before capacity degradation. *Nature Energy*, 4(5):383–391.

Singh, P., Kaneria, S., Broadhead, J., Wang, X., and Burdick, J. (2004). Fuzzy logic estimation of soh of 125ah vrla batteries. In *INTELEC 2004. 26th Annual International Telecommunications Energy Conference*, pages 524–531. IEEE.

Smola, A. J. and Schölkopf, B. (2004). A tutorial on support vector regression. *Statistics and computing*, 14(3):199–222.

Spitthoff, L., Shearing, P. R., and Burheim, O. S. (2021). Temperature, ageing and thermal management of lithium-ion batteries. *Energies*, 14(5):1248.

Sun, H., Jiang, B., You, H., Yang, B., Wang, X., Wei, X., and Dai, H. (2021). Quantitative analysis of degradation modes of lithium-ion battery under different operating conditions. *Energies*, 14(2):350.

Tan, X., Tan, Y., Zhan, D., Yu, Z., Fan, Y., Qiu, J., and Li, J. (2020). Real-time state-of-health estimation of lithium-ion batteries based on the equivalent internal resistance. *Ieee Access*, 8:56811–56822.

Vetter, J., Novák, P., Wagner, M. R., Veit, C., Möller, K.-C., Besenhard, J., Winter, M., Wohlfahrt-Mehrens, M., Vogler, C., and Hammouche, A. (2005). Ageing mechanisms in lithium-ion batteries. *Journal of power sources*, 147(1-2):269–281.

Virtanen, P., Gommers, R., Oliphant, T. E., Haberland, M., Reddy, T., Cournapeau, D., Burovski, E., Peterson, P., Weckesser, W., Bright, J., van der Walt, S. J., Brett, M., Wilson, J., Millman, K. J., Mayorov, N., Nelson, A. R. J., Jones, E., Kern, R., Larson, E., Carey, C. J., Polat, İ., Feng, Y., Moore, E. W., VanderPlas, J., Laxalde, D., Perktold, J., Cimrman, R., Henriksen, I., Quintero, E. A., Harris, C. R., Archibald, A. M., Ribeiro, A. H., Pedregosa, F., van Mulbregt, P., and SciPy 1.0 Contributors (2020). SciPy 1.0: Fundamental Algorithms for Scientific Computing in Python. *Nature Methods*, 17:261–272.

Waag, W., Käbitz, S., and Sauer, D. U. (2013). Experimental investigation of the lithium-ion battery impedance characteristic at various conditions and aging states and its influence on the application. *Applied energy*, 102:885–897.

Wikner, E. (2019). *Ageing in Commercial Li-ion Batteries: Lifetime Testing and Modelling for Electrified Vehicle Applications*. Chalmers University of Technology.

Wikner, E., Björklund, E., Fridner, J., Brandell, D., and Thiringer, T. (2021). How the utilised soc window in commercial li-ion pouch cells influence battery ageing. *Journal of Power Sources Advances*, 8:100054.

Yang, Q., Xu, J., Li, X., Xu, D., and Cao, B. (2020). State-of-health estimation of lithium-ion battery based on fractional impedance model and interval capacity. *International Journal of Electrical Power & Energy Systems*, 119:105883.

Zhang, Y. and Wang, C.-Y. (2009). Cycle-life characterization of automotive lithium-ion batteries with linio2 cathode. *Journal of the Electrochemical Society*, 156(7):A527.

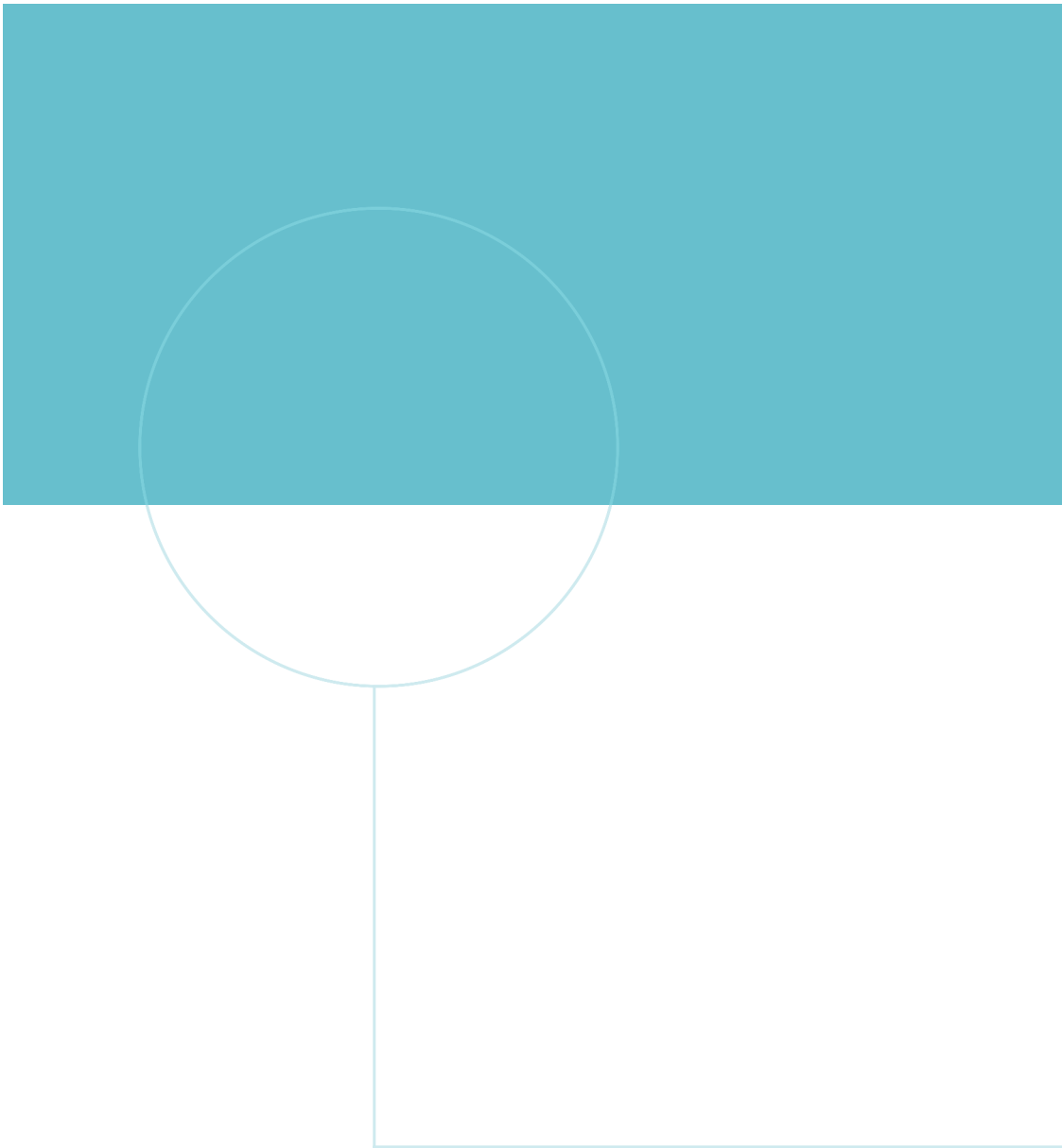

NTNU

Norwegian University of
Science and Technology